# Deliverable D5-2
# Best Practice Guide on characterisation of components of free-space QKD systems

**[PTB,** CMI, INRIM, Aalto, Metrosert, NPL, PoliMi, Toshiba, TUB,
IDQ, KRISS, METAS, MPD, UniGE CH**]**

***Delivery date as per Annex 1:*** *May 2018 (M36)*
***Actual delivery date:*** *May 2018 (M36)*

# Measurement facilities for detectors for free-space QKD

## *Use of a thermally cooled miniature Si photodiode reflection trap for measurement of detection efficiency (DE) and linearity of free space single photon detectors in NIR wavelength range*

### Objective

In studies of the properites of free-space single photon detectors, e.g. detection efficiency (DE) and linearity, often small beam diameters and low noise at low photon fluxes are required. For that purpose, a thermally cooled miniature Si-photodiode reflection trap in conjunction with custom-made high-sensitivity readout electronics can be used.

### Device

In the following we describe, as an example, the miniature trap detector realized in the MIQC2 project, where the Silicon-based photodiodes of type HPN S1337-33BQ SPL (windowless) from Hamamatsu are used. Those photodiodes have a relatively small active area of (2.4x2.4) mm$^2$ which is protected with antireflection $SiO_2$ coating of nominal thickness $t$=30 nm. In the trap detector three photodiodes are assembled in the polarization-independent configuration [1] (Figure 1). The outer dimensions of the housing: external diameter 35 mm, length 45,5 mm (excl connectors).

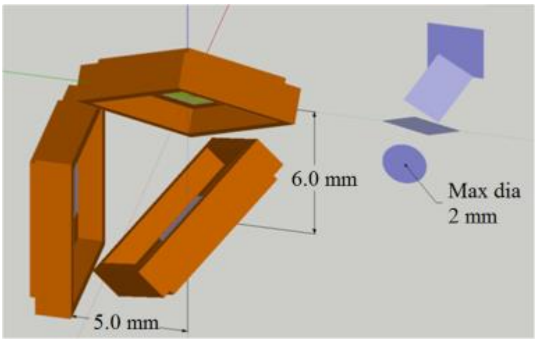


*Figure 1: Arrangement of photodiodes in the miniature trap detector (leftmost) providing approximately circular-shaped maximum active area of the whole detector with about 2 mm in diameter (rightmost) [2].*

To convert the photocurrent generated by the photodiodes in the trap detector to a measurable voltage signal a switched integrator amplifier (SIA) is used. The SIA stores the photocurrent's charge in a capacitor $C$ for a defined amount of time $t_{int}$. The longer is the integration time, the higher is the SIA voltage output $V_{out}$ (Figure 2).

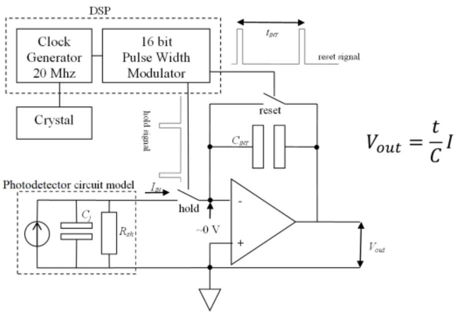


*Figure 2: Principle lay-out of switched integration amplifier [32].*

### Performance

For the best noise performance, it is recommended to integrate the analogue part of SIA inside the mini trap housing (Figure 3). This will reduce noise due to connection cables and keeps the cooled trap detector and the SIA at approximately the same temperature conditions.

One of the important characteristics is the capacitor value, because it defines the dynamic range of the SIA. For example, when using an integration capacitor of 10 pF the conversion factor I/V ranges from $1x10^7$ to $1x10^{11}$ varying the integration time from $1x10^{-3}$ to 1 s. The duration of integration time can be optimized according to the optical power level measured. At the highest sensitivity the noise equivalent power (NEP) of the mini-trap in conjunction with SIA was measured to be as low as 10 fW/Hz$^{½}$ at the wavelength of 850 nm.

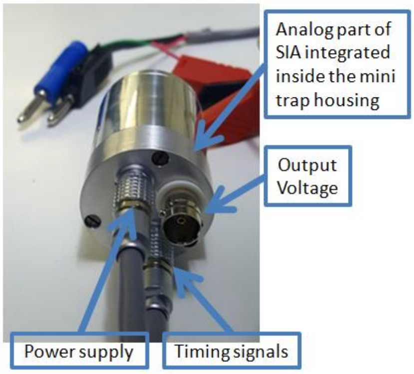


*Figure 3. Integrated analogue part of SIA inside the mini trap housing.*

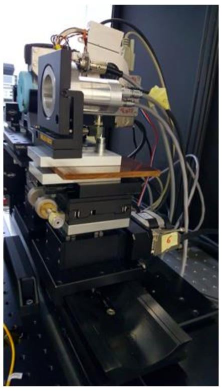

*Figure 4. Calibration arrangement at CMI for comparison of transfer trap detector (blue coloured, leftmost) and the mini-trap detector with SIA (rightmost).*

The completed photodetector should be calibrated for responsivity by using well-established measurement set-up [4] to obtain the desired uncertainty. The calibration is conducted either against a cryogenic radiometer [5] or a transfer standard detector (Figure 4). In the calibration set-up, the alignment of the detector is of utmost importance and for reflection trap detectors, typically, it is observed that the back-reflected beam from the device travels along the impinging beam. With the mini-trap the correct alignment is challenging because its small active area is hidden in the housing. On the other hand, the benefit of using photodetector in trap configuration is that the undesired influence of the back-reflected beam in measurements (e.g. entering fore-optics etc) is reduced in about three orders of magnitude.

If well-aligned, beams of small diameter can be fit and measured with the completed mini-trap detector. For example, the measurements conducted at Czech Metrology Institute (CMI) indicated that a beam with diameter 50 um is possible. During measurements performed at 850-nm wavelength the ratio of responsivity between mini-trap in conjunction with SIA and CMI 3-element transfer standard trap (which is traceable to the cryogenic radiometer) was determined very close to unity, i.e. 0.9995.

In summary, such a thermally cooled miniature Si-photodiode reflection trap in conjunction with custom-made high-sensitivity readout electronics is able to perform at about $5x10^3$ photons/s/Hz$^{1/2}$ noise equivalent in the NIR wavelength range.

## ***References***

[1] N. P. Fox, Trap detectors and their properties, Metrologia 28, 197-202, 1991.

[2] A. Pokatilov, M. Parker, T. Kübarsepp, G. Porrovecchio, M. Šmid, A. Vaigu and S. Kück, Low-noise miniature photodetector as a transfer standard for SPAD calibration in the visible wavelength range, Proc. of NEWRAD 2017 (Tokyo, Japan, 2017).

[3] G Porrovecchio, M. Šmid, M. López, H. Hofer, B. Rodiek and S Kück, Comparison at the sub-100 fW optical power level of calibrating a single-photon detector using a high-sensitive, low noise silicon photodiode and the double attenuator technique, Metrologia, 53, 1115–1122, 2016.

[4] Look at Section „Use of a double monochromator-based calibration facility to perform spectral characterisation of DE, linearity and spatial uniformity in free space (CMI)".

[5] J. E. Martin, N. P. Fox, P. J. Key, "A cryogenic radiometer for absolute radiometric measurements," Metrologia 21, 147-155 (1985).

## *Use of a laser-based facility for the calibration of the detection efficiency of single-photon detectors using in-situ calibrated neutral density filters and an attenuator based on Si-photodiodes in trap configuration*

### *Introduction*

Silicon Single-Photon Avalanche Diodes (Si-SPADs) gain importance in a variety of different fields of scientific research, i.e. experimental quantum optics, quantum cryptography and quantum computing, but also in medicine, biology and astrophysics. Since several years, these diodes are commercially available. The detection efficiency of these devices is one of the most important parameters for application, besides characteristics like detection jitter, dead time and after-pulsing probability, see e.g. the overview article about metrology of single-photon sources and detectors by Chunnilall et al. [1].

Measurements of the absolute detection efficiency of photon-counting devices, based on two photon correlation techniques and on comparison to classically calibrated detectors, have been carried out since several years, see e.g. [2]. For the photon correlation technique, a calibrated standard detector is principally not needed and thus also no traceability to an absolute detector is necessary. However, from a metrological point of view, a validation with a standard detector traceable to the cryogenic radiometer or to a calibrated lamp is necessary, because otherwise two independent scales for the optical power would exist. Thus, conventional calibration methods (usually traceable to a cryogenic radiometer or a standard lamp) for validation were carried out, e.g. see Migdall et al. [2] and references therein.

For the calibration a laser source is used, therefore the Poissonian photon number distribution has to be taken into account in the calibration process, as investigated in the work of Schmunk et al. [3]. Depending on the attenuation, the mean photon number applied to the detector varies in a wide range, thus in combination with the detector dead time this leads to a strong dependence of the measured detection efficiency from the incoming photon flux.

This best practice guide is based on the work presented in [4] and [5].

### *Calibration setup and procedure*

In the setup presented in the paper, the calibration of a Si-SPAD (Perkin-Elmer-SPCM-AQR-16) is carried out via comparison with a calibrated Si-diode (Hamamatsu S1227), which acts as the reference detector, using a continuous wave laser source operating at 770 nm. This comparison is not possible to perform directly, because of the different photon fluxes that need to be applied to the detectors. This is taken care of by using appropriate neutral density filters, which are calibrated in-situ in the same setup. However, the attenuation of such a filter has to be in the order of $10^7$ to $10^8$ in order to attenuate the incoming photon flux from the laser down to single-photon level. Such a high attenuation is practically not possible to be measured with a standard Si-diode, because in this case the photon flux is simply too small. To overcome this problem, the following procedure was used and implemented in the setup shown in Figure 1. The power of a stabilized diode laser operating at a wavelength of 770 nm is directly measured with the standard Si-diode. Then, a filter 2 (NG9, OD5.0, $T \sim 4.6 \times 10^{-4}$) is moved into the beam and the corresponding power is also measured with the standard Si-diode. The same procedure is repeated for filter 3 (Filter package consisting of NG9, OD2.6 and NG9, OD3.0, total transmittance $\sim 1.6 \times 10^{-4}$). For the translation of the neutral density filters, computer-controlled translation stages with an accuracy of 1 µm were used, so that the filters were always irradiated at the same position, thus avoiding effects of filter inhomogeneity. Therefore, highly accurate in-situ measurements of the filter transmissions of filter 2 and filter 3 are performed. However, the effect of combining two filters, which is necessary for the measurement with the Si-SPAD detector, still has to be taken into account. For the validation of the applicability of the above described procedure and a discussion of associated uncertainty of the filter transmission. In the final step of the calibration procedure, now both filter simultaneously as well as the Si-SPAD are moved into the beam. From the known laser power and the measured filter transmissions the incoming photon flux onto the Si-SPAD is now known and thus the detection efficiency can be determined. For varying the laser power and thus the photon rate impinging on the detector, an additional variable filter (Thorlabs, NDL-10S-4, with optical densities between 0.1 and 4) was placed right in front of the laser. This filter has no further effect on the measurement other than changing the radiative flux. Because the laser itself could the operated at the same power level, the radiative flux is much more stable than in the case where the radiative flux was changed by adjusting the operational conditions of the laser. It should be noted, that both detectors, the standard Si-diode as well as the Si-SPAD are underfilled by the incoming beam, this is assured by the use a microscope objective (Mitutoyo M Plan Apo, 20x, NA = 0.42), which remains in the beam throughout the whole calibration procedure.

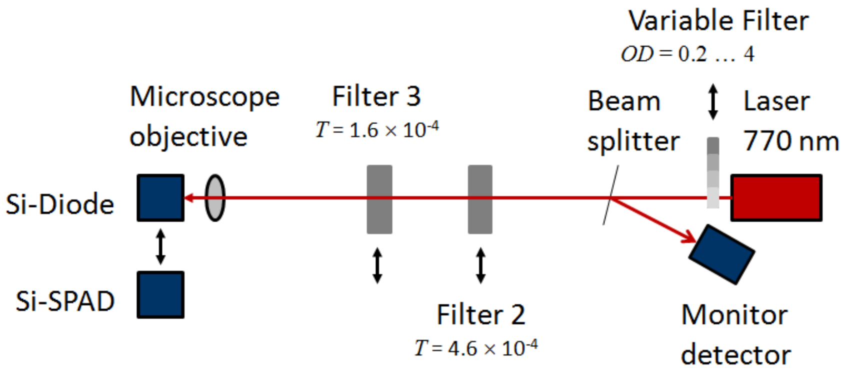


*Figure 1a: Schematic setup for the detection efficiency calibration of Si-SPADs.*

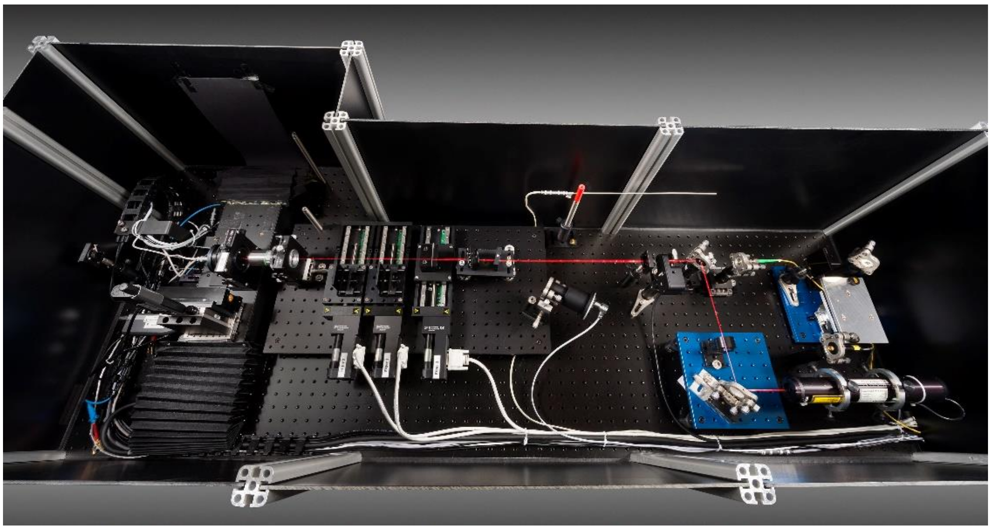

*Figure 1b: Photograph of setup for Si-SPAD detector calibration.*

## ***Determination of the detection efficiency***

In the procedure described above, the following four signals $V_1$ to $V_4$ are measured:

$$\left.\begin{aligned}
V_1 &= A_1 \cdot s_{\mathrm{Si},1} \cdot \Phi_1 \\
V_2 &= A_2 \cdot s_{\mathrm{Si},2} \cdot \Phi_2 = A_2 \cdot s_{\mathrm{Si},2} \cdot T_{\mathrm{F2}} \cdot \Phi_1 \\
V_3 &= A_3 \cdot s_{\mathrm{Si},3} \cdot \Phi_3 = A_3 \cdot s_{\mathrm{Si},3} \cdot T_{\mathrm{F3}} \cdot \Phi_1 \\
V_4 &= CR = \eta \cdot \frac{\Phi_4}{hc/\lambda} = \eta \cdot \frac{T_{\mathrm{F2}} \cdot T_{\mathrm{F3}} \cdot \Phi_1}{hc/\lambda}
\end{aligned}\right\}$$

$$\Rightarrow \eta = hc/\lambda \cdot \frac{A_2 \cdot A_3 \cdot}{A_1 \cdot} \cdot \frac{CR \cdot V_1}{V_2 \cdot V_3} \cdot \frac{s_{\mathrm{Si},2} \cdot s_{\mathrm{Si},3}}{s_{\mathrm{Si},1}} \tag{1}$$

With: $\eta$: detection efficiency, $V_\mathrm{i}$: signals ($V_1$: signal for the measurement of the laser power, $V_2$: signal for the measurement of filter 2, $V_3$: signal for the measurement of filter 3, $V_4$: signal (= count rate $CR$) for the measurement with the Si-SPAD, $s_{\mathrm{Si,i}}$: spectral responsivitiy of the Si-diode for the different irradiation levels, $A_\mathrm{i}$: amplification factors of the transimpedance amplifier in the measurements 1 – 3, $\Phi_\mathrm{i}$: radiant powers, $T_{\mathrm{F2}}$, $T_{\mathrm{F3}}$: filter transmissions, $CR$: count rate of the Si-SPAD, $h$: Planck constant, $c$: speed of light and $\lambda$: wavelength. It should be noted that the detection efficiency is defined here purely as the number of counts divided by the number of impinging photons, i.e. other effects, as e.g. after-pulsing, are not considered.

This equation is valid only, if the laser power does not change during the measurements. This is taken into account by applying the monitor principle in the measurements. This means, that instead of using the signals directly, the ratios $Q_\mathrm{i}$ between the measured signals $V_\mathrm{i}$ and the simultaneously measured monitor signals $V_{\mathrm{mon,i}}$ are used. Furthermore, the responsivities of the Si-diode is practically linear for the applied power levels between approx. 1 nW and 10 µW (the dynamic range of this type of diode is approx. 3 pW … 300 µW) and thus taken into account by an uncertainty component, see section 4. So, the following equation for the detection efficiency is finally obtained:

$$\begin{aligned}
\eta &= \frac{hc}{\lambda} \frac{A_2 A_3}{A_1} \frac{V_1/V_{\mathrm{Mon1}} \; CR/V_{\mathrm{Mon4}}}{V_2/V_{\mathrm{Mon2}} \; V_3/V_{\mathrm{Mon3}}} s_{Si} F_{\mathrm{filt}} \\
&= \frac{hc}{\lambda} \frac{A_2 A_3}{A_1} \frac{Q_1 Q_4}{Q_2 Q_3} s_{Si} F_{\mathrm{filt}}
\end{aligned} \tag{2}$$

With $F_{\mathrm{filt}} = 1 \pm u(F_{\mathrm{filt}})$: uncertainty related to the filter transmission determination, see section 4.

## ***Optimization***

The optimization of the above described procedure were described in detail in [5]. These optimizations are based on the following changes:

1. Optimization of the Si-SPAD detector positioning using an automated procedure and thus diminishing the effect of inhomogeneity on the calibration result.
2. Reduction of the uncertainty contribution due to the filter transmission measurement by using an integrating sphere, which diminishes the back reflection into the measurement setup.

## ***References***

[1] C. J. Chunnilall, I. P. Degiovanni, S. Kück, I. Müller, A. G. Sinclair; “Metrology of single-photon sources and detectors: a review” Opt. Eng. 0001;53(8):081910. doi:10.1117/1.OE.53.8.081910 (2014).

[2] Single-Photon Generation and Detection, Volume 45: Physics and Applications (Experimental Methods in the Physical Sciences), edited by: Alan Migdall, Sergey V. Polyakov, Jingyun Fan, Joshua C. Bienfang, ISBN-13: 978-0123876959, ISBN-10: 0123876958, Academic Press, 2013.

[3] W. Schmunk et al., "Radiometric Calibration of Single Photon Detectors by a Single Photon Source based on NV-centers in diamond", Journal of Modern Optics 58, 1252 (2011)

[4] M. López, H. Hofer, S. Kück, "Detection efficiency calibration of single-photon silicon avalanche photodiodes traceable using double attenuator technique, Journal of Modern Optics 62, S21 – S27 (2015), http://dx.doi.org/10.1080/09500340.2015.1021724.

[5] K. Dhoska, H. Hofer, B. Rodiek, M. López, T. Kübarsepp, S. Kück, "Alignment position method for SPAD detector calibration and homogeneity", International Journal of Scientific Reports, 1, 271 – 274, 2015, doi: http://dx.doi.org/10.18203/issn.2454-2156.IntJSciRep20151253.

## *Use of a measurement system for determining the detection efficiency of a TES detector system*

This guide describes the characterization of fiber-coupled Transition-Edge Sensor (TES) single photon counters in terms of their detection efficiency (DE). The DE is defined as the probability of a single photon present in the optical fiber routed to the TES to be detected. The DE measurements have been demonstrated on a detection system employing W-TES-based single photon counters [1,2] that has been set up within the EMPIR project "*MIQC2* - Optical metrology for quantum-enhanced secure telecommunication" [3]. Further details of the detection system and its application to characterize the photon statistics of quantum light sources are described in [4].

### ***Basic concept***

The DE measurement is based on the comparison of an optical power measurement in the mW-range with the rate or number of single photons detected by the TES detector. A simplified procedure compared to previously reported DE-measurements of fiber-coupled TES single photon counters has been used [1,5].

The basic DE measurement configuration is depicted in Figure 1b. A laser source operated in cw-mode is employed to produce an optical test signal of Poissonian photon emission distribution. The laser output is fed to the input port of an optical fiber-coupled beam splitter with two output ports. One output port (A) of the beam splitter is routed to a calibrated absolute power meter (PM). The cw optical power *P* is obtained from the power meter measurement. The second output port (B) of the beam splitter is connected to the input of a fiber-coupled attenuator. The attenuation of this element is chosen so that the optical power at its output port is in the single-to-few photon level. The attenuator output is connected via a spliced fiber connection to the TES detector. During the DE measurement, the power *P* is continuously measured.

It is evident from this configuration that to extract the DE from a comparison of the optical power *P* and the number/rate of single photons detected by the TES knowledge of the split ratio *r* of the outputs A and B is required. Hence, this split ratio is measured separately again employing a calibrated absolute power meter, as depicted in Figure 1a. It is assumed that the split ratio *r* is independent of the optical power used for this measurement. Therefore, the power level used here should be chosen so that the spilt ratio *r* is determined with lowest achievable uncertainty of the calibrated absolute power meter.

The principle measurement configuration in Figure 1b can be used in cw-mode as well as in so-called pulsed-mode. Implementations of the two modes are discussed in the following sections.

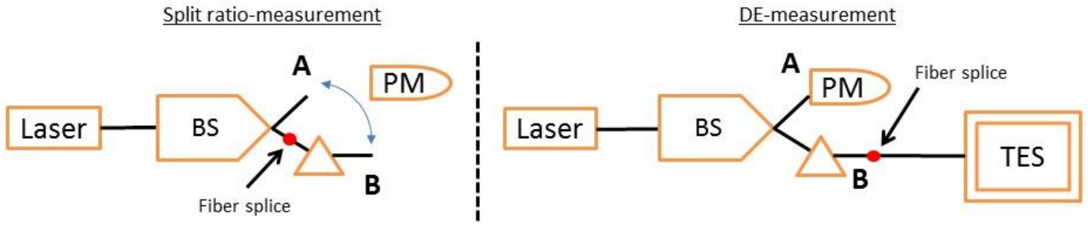


*Figure 1 Measurement of the detection efficiency in an optical fibre-coupled configuration. Left: the split ratio r of output A and B of a fibre beam splitter is determined using a calibrated absolute power meter. Right: port A is used to monitor the power, port B is spliced to the fibre routed to the TES detector.*

### ***CW-mode***

The basic principle of measuring DE in cw mode is to count the number of *single* photons detected by the TES in a fixed time interval to determine the detected single photon rate *d*. Here, it is important to ensure that the incident photon rate should not exceed a level that would result in a high probability of absorbing multiple photons (so-called pile-up events) within the characteristic recovery time of TES-based optical photon counters, typically of order 1 microsecond. Given the Poissonian photon emission statistics of the laser source, the probability *P* of *n* photons occurring within the time interval $\Delta t$ follows the relation

$$P_n(\Delta t) = (\langle n \rangle^n / n!) e^{-\langle n \rangle} \qquad (1)$$

with $\langle n \rangle = d\Delta t$ as the average photon number. Consequently, at a photon rate d = 10 kHz the probability of one and two photons occurring within time interval $\Delta t$ = 1 µs is 1e-2 and 5e-5.

It is advisable to employ a variable attenuator placed between the laser output and the beam splitter input port for the DE measurement in cw mode, as depicted in Figure2. This way, the incident photon rate and the probability of (undetected) pile-up events can be adjusted *in situ*.

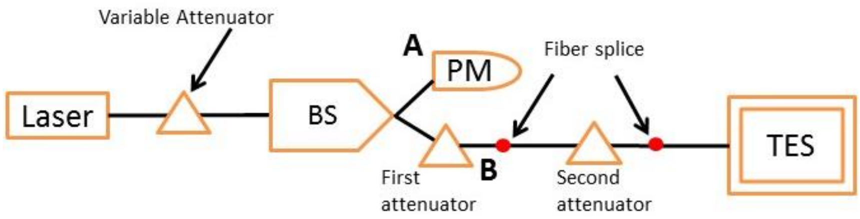


*Figure 2: DE measurement in cw-mode: a CW laser is power-attenuated from the mW-regime to the single-to-few photon level using a fiber-based attenuator cascade consisting of a beam splitter and a first and second attenuator. A variable attenuator is used to adjust the photon rate.*

It may be necessary to further reduce the incident photon rate. For this purpose, a second fiber-coupled attenuator of fixed attenuation can be inserted between the output port B and the TES detector, as shown in Figure 2. The determination of the attenuation b of the second attenuator would be performed with the calibrated absolute power meter. Again, the power level should be chosen so that value of *b* is determined with lowest achievable uncertainty of the power meter.

The DE measurement in cw-mode is analyzed using the relation

$$\eta = \frac{d \cdot h \cdot c \cdot r \cdot b}{\lambda \cdot P} \tag{2}$$

with $\eta$ - detection efficiency, d - detected single photon rate, *h* - Planck‘s constant, *c* - speed of light, *r* – split ratio, $\lambda$ - photon wave length, *P* - cw optical power at port A, and -if used- *b* – attenuation of the second attenuator. The power level *P* is continuously measured. Additionally, it is advisable to monitor $\lambda$ via a wavelength meter.

The detected single photon rate *d* is obtained from the analysis of digitized TES detector output signal time series. A representative time series is shown in Figure3. The analysis firstly concerns finding a trigger level that ensures a reliable discrimination between single photon detection signals and the detector noise band. This is illustrated in Figure3. The trigger level is varied from within the detector noise band towards larger signal values. Basic pulse height analysis of the signal is performed every time the signal level exceeds the trigger level. This way the pulse heights of ‘noise events’ as well as of the sought single photon detection signals are obtained. The pulse heights are then histogrammed with respect to the trigger level, see Figure3. Noise events and single photon detection signals are identified as being below and above a region in the histogram of vanishing counts. The so-called optimal trigger level is obtained from this region in the histogram.

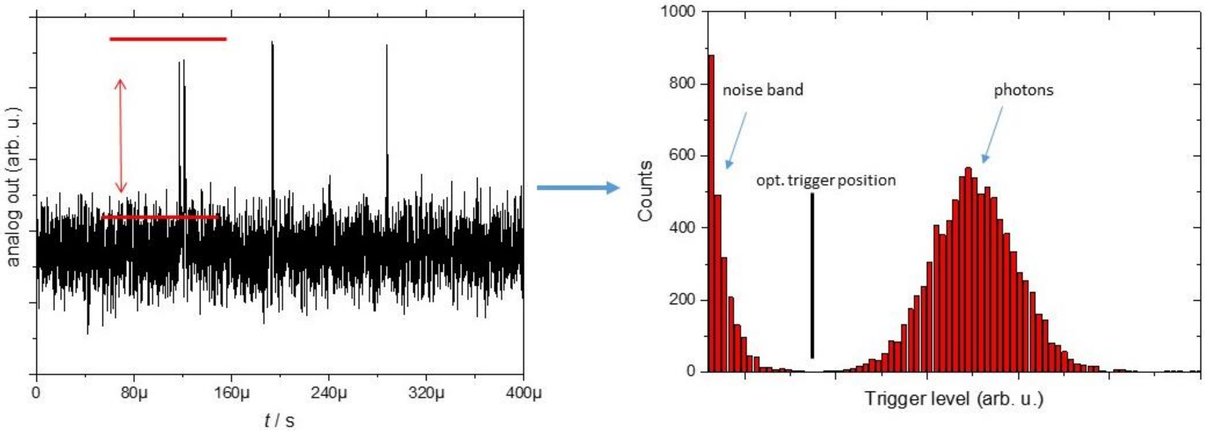


*Figure 3: Determination of the optimal trigger level for cw-mode analysis: pulse heights were determined from the time signal and histogrammed to find the optimal trigger position between noise band and photon events.*

The optimal trigger level is then used to re-analyze the TES detector output signal time series. This analysis includes a *varied dead time* approach. The dead time $t_{dead}$ is a time interval within which a triggered TES detector output signal is *not* accepted as originating from a single photon detection, it is illustrated in Figure4. If $t_{dead}$ is significantly shorter or of order of the characteristic TES recovery time, the triggered detector signals cannot originate from subsequent single photon absorptions. Triggering can, however be caused, e.g., by the falling branch of the TES signal pulse. Therefore, the signal time series are analyzed for varying values of time $t_{dead}$ after the signal level exceeds the optimal trigger level.

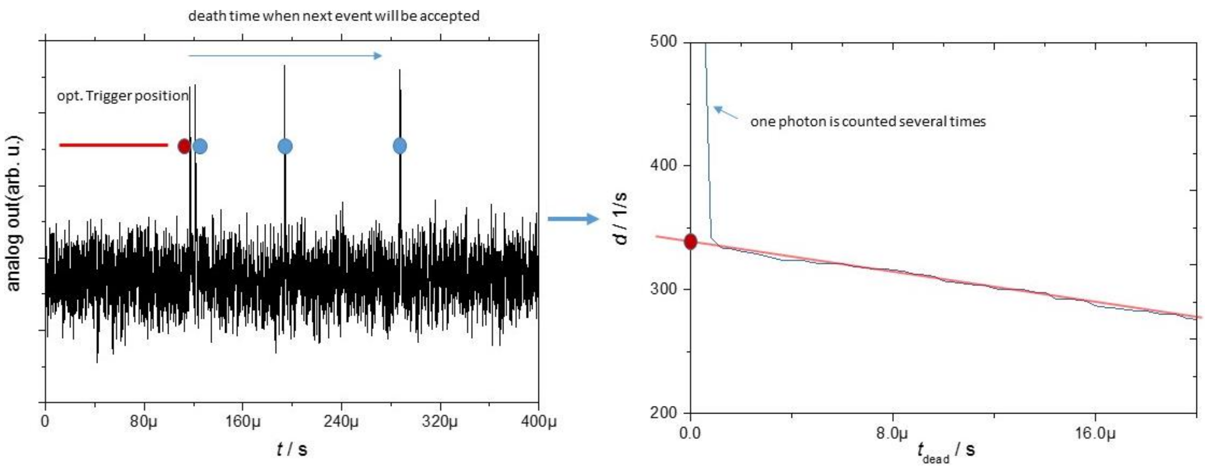


*Figure 4: Variable dead time approach to determine the true photon rate for cw-mode analysis Left: the time signals are analyzed several times and at the same time the acceptance window (dead time) is varied. Right: the apparent single photon detection rate d is extrapolated towards tdead $\rightarrow$ 0, the value at the y-axis intercept is taken as the true single photon detection rate.*

This means that subsequent trigger thresholds for a given value of $t_{dead}$ are only accepted for $t > t_{dead}$. This way values for the detected single photon rate $d$ for the varied dead times $t_{dead}$ are obtained. A representative plot of $d$ vs. $t_{dead}$ is shown in Figure4. It can be seen that (i) the apparent single photon detection rate strongly increases for $t_{dead}$ values approaching the TES recovery time and (ii) that the apparent rate is not constant for larger $t_{dead}$ values but slightly decreasing. In order to obtain a reliable estimate of the single photon detection rate of the TES, the values of the apparent rate for larger $t_{dead}$ values is extrapolated towards $t_{dead} \rightarrow 0$. The value of $d$ at the y-axis intercept of the extrapolated curve $d$ vs. $t_{dead}$ is taken as the *true* single photon detection rate and used in the above calculation of the quantum efficiency.

The main uncertainty contributions to the values of $\eta$ obtained in cw-mode arise from the single photon detection rate $u_d$ (type A), the power level at port A $u_P$ (type B), the split ratio $u_r$ (type B) as well as the second attenuator $u_b$ (type B), if used. Furthermore, parasitic ambient light can affect the cw-mode measurement and would apparently increase the photon detection rate and, hence, result in an overestimation of the quantum efficiency. This issue can be significantly mitigated by means of a pulsed method discussed in the following section.

## ***Pulsed mode***

The setup for the DE measurement in pulsed mode is shown in Figure5. The main difference to the cw-mode configuration is that a fiber-based electro-optical modulator (EOM) is placed in between the laser output and the input of the fiber beam splitter. The EOM enables to define pulses with a known length $l$ by switching its state from transmitting ('zero biased') to deflecting, i.e. non-transmitting. The choice of $l$ in combination with the laser power and split ratio defines the mean photon numbers per pulse $\mu_{\mathrm{Fiber}}$ in the optical fiber routed to the TES detector. The TES detector signal acquisition is synchronized to the well-defined timing of the pulse sequence. This way parasitic ambient light effects are practically eliminated. Furthermore, the pulse rate can be easily modified *in situ*. This way, the EOM is used as a variable attenuator in the time domain and, hence, an additional variable attenuator is not necessary. The DE measurement of the two W-TES-based single photon counters used in the detection system set up within *MIQC2* is detailed below.

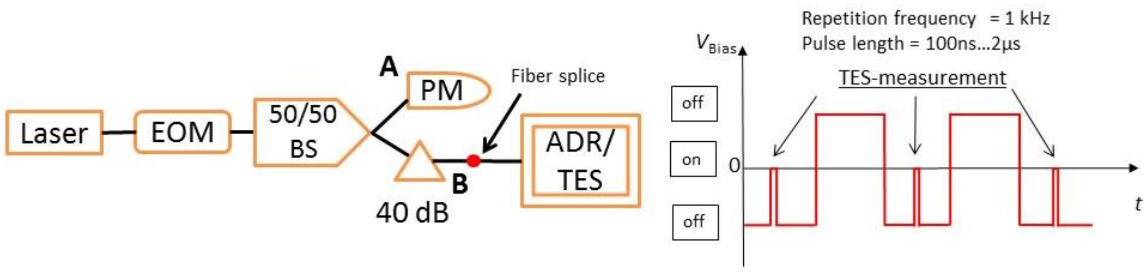


*Figure 5: DE measurement in pulsed mode. Left: an EOM is used to define pulses from a CW Laser. The light is guided through an attenuator cascade and weakened to the single-to-few photons per pulse level. Port A is used to monitor the power, and port B is spliced to the TES fiber. Right: schematic of the EOM bias waveform. The light pulses are defined by the dwell time at zero bias, and the data acquisition of the TES signal is synchronized to the pulse sequence. The average EOM bias voltage is close to zero to prevent polarization effects of the EOM crystal.*

The cw laser ($\lambda$ = 932nm) output is connected via the EOM to the attenuator cascade consisting of a 50/50 beam splitter and a 40-dB attenuator spliced to one of its two output ports. The split ratio $r$ of output A and B has been determined before using a calibrated power meter, the same way as described for the cw-mode. The EOM is used to define pulses with a length of $l$ = 100 ns to 2 µs corresponding to mean photon numbers per pulse $\mu_{\mathrm{Fiber}}$ in the range between 0.1 and 2. It has an insertion loss of 4.3dB and an extinction ratio between its deflecting state and its transmitting state of $\sim$1000.

The DE measurement is performed in two steps: The first step is to measure the cw power $P$ of the laser present at input A. During this measurement, the EOM is permanently in the transmitting zero bias state. This measurement is taken using a calibrated absolute power meter , which is traceable to a cryogenic radiometer. This measurement has a relative standard uncertainty of 0.3%. This uncertainty (type B) includes reflection losses at the output A and represents a lower bound of the total uncertainty of the DE measurement in pulsed mode. The second step is to measure the photon number in the light pulses with the TES. Here, the EOM is driven by a waveform at a repetition frequency of $\sim$kHz that is schematically depicted in Figure 5. The square wave has a duty cycle close to 50% and is chosen so that the average EOM bias voltage nearly vanishes. This is done to prevent drift effects of the EOM. Start, stop and length of the light pulses are defined by the dwell time at zero EOM bias. Data acquisition of the TES signal is synchronized to the pulse sequence. Each individual TES signal trace has a length of 10 microseconds and is recorded with a sampling rate of 125 MS/s. Data sets for a total number of $N$ pulses are obtained. The presence and number of photons is determined from the maximum level of the TES signal trace relative to the signal baseline. The TES signal-to-noise ratio for the detection of 1 photon at $\lambda$ = 932nm for the two W-TES-based single photon counters used in the detection system is >4 [4]. Hence, determining both the presence and the number of photons per pulse is reliably possible. The number of detected photons per pulse is then histogrammed, as shown in Figure6. The histogram shows that the number of pulses *without* detected photons can be accurately determined.

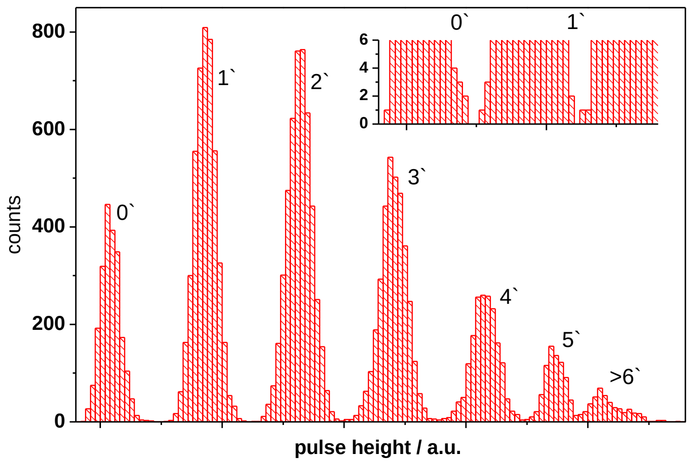


*Figure 6: Analysis of DE measurement in pulsed mode. The number of TES signal traces with 0, 1, … >6 detected photons per pulse is histogrammed. The inset shows the region between 0 and 1 photon per pulse.*

The DE measurement in pulsed mode is analyzed using the relation

$$\eta = \frac{-\ln\left(\frac{N_0}{N}\right) \cdot h \cdot c \cdot r}{\lambda \cdot P \cdot l},$$

with $\eta$ - detection efficiency, $h$ - Planck's constant, $c$ - speed of light, $r$ - split ratio, $\lambda$ - photon wavelength, $P$ - cw optical power at port A, $l$ - pulse length, $N$ - total number of pulses and $N_0$ - number of pulses without detected photons. This relation is based on the Poissonian photon emission statistics of the laser source [1]. Both measurement steps are repeated alternately, and additionally the wavelength $\lambda$ is continuously monitored via a wavelength-meter with an accuracy of 1.7 pm. From measurement data sets with the total number of pulses $N$ = 40.000 detection efficiencies of 0.8877 ± 0.0066 and 0.8749 ± 0.0066 for the two W-TES-based single photon counters used in the detection system are obtained. The stated standard uncertainties $u$ ($k$ = 1) comprise mainly contributions from the total number of pulses $u_N$ = 0.0043 (type A), the power level at port A $u_P$ = 0.0033 (type B) and the split ratio $u_r$ = 0.0038 (type B).

## ***Summary***

The detection efficiency of fiber-coupled Transition-Edge Sensor single photon counters can be determined by comparing an optical power in the mW-range with the rate (cw-mode) or number (pulsed mode) of single photons detected by the photon counter. A source of optical test signals with known, e.g., Poissonian photon emission distribution, state-of-the-art fiber-coupled beam splitters and attenuators with high and precisely know attenuation factors as well as an absolute optical power meter are key elements of the DE measurement. For the DE measurement in pulsed mode an optical modulator is required to define pulses of known length $l$ that is less or of order of the characteristic TES recovery time.

A DE measurement with a total relative standard measurement uncertainty < 1% has been demonstrated on a detection system employing W-TES-based single photon counters. This measurement has been performed in pulsed mode to mitigate measurement errors arising from parasitic ambient light. A fiber-based electro-optical modulator operated in a bias scheme preventing drift effects was used. Detection efficiencies for the two detectors of 0.8877 ± 0.0066 and 0.8749 ± 0.0066 have been observed, respectively. Possible explanations for the slightly lower values compared to previously published results [5,6] on very similar TES detectors are the reflection losses at $\lambda$ = 932nm, because the TESs are optimized for 1064 nm, as well as parasitic losses from the splice connections in the TES fiber link. Another potential source is reflection losses at the unterminated end face of the fiber ferrule used in the detection system.

## ***References***


[1] A.E. Lita, A.J. Miller, S.W. Nam, Opt. Express 16, 3032–3040 (2008)

[2] A.J.Miller, A.E. Lita, B. Calkins, I.Vayshenker, S.M.Gruber, S.W.Nam,Opt. Express 19, 9102 (2011)

[3] http://empir.npl.co.uk/miqc2/project/

[4] M. Schmidt, M. v. Helversen, M. López, F. Gericke, E. Schlottmann, T. Heindel, S. Kück, S. Reitzenstein, and J. Beyer, Photon-number-resolving transition-edge sensors for the metrology of quantum light sources, J. Low Temp. Phys., DOI: 10.1007/s10909-018-1932-1 (2018)

[5] A.E. Lita, B. Calkins, L.A. Pellouchoud, A.J. Miller, S.W. Nam, SPIE 4, 7681 (2010)

[6] D. Fukuda, G. Fujii, T. Numata, K. Amemiya, A. Yoshizawa, H. Tsuchida, H. Fujino, H. Ishii, T. Itatani, S. Inoue, T. Zama, SPIE 4, 7681 (2010)

# Measurement facilities for sources used in free-space QKD

## *How to measure the mean number of photons and the photon distribution functions of a pseudo-single-photon-source suitable for open air QKD?*

### ***Introduction***

In a pulsed-laser source, used typically in the implementation of quantum key distribution (QKD), the probability of producing an $n$-photon state $|n\rangle$ is a Poisson distribution $P(n) = (\mu^n/n!)e^{-\mu}$, where $\mu = \langle n \rangle$ is the mean number of the photon per pulse [1-2]. In this section, the measurement procedure and setup for determining the mean photon number and the photon distribution of a QKD source is reported.

### ***Measurement procedure***

The mean photon number per laser pulse $\mu$ can be obtained either by using a traceable single photon detector; e.g. a SPAD detector, SNSPD-Detector, TES Detector, etc. or by using a traceable analogue detector (semiconductor detector, e.g. Si, Ge or InGaAs photodiode). On one hand, when a single-photon detector (SPAD) is used, the mean photo number $\mu$ of a laser pulse is obtained by,

$$\mu = \frac{P_i - P_d}{\eta} \cdot \frac{1}{1 + P_{after}} \tag{1}$$

where $\eta$ is the detection efficiency, $P_i$ is the count probability, $P_d$ is the dark count probability and $P_{after}$ is the after-pulse probability. On the other hand, the mean photon number per laser pulse $\mu$ using an analogue detector is obtained by,

$$\mu = \frac{P}{f_{rep} \cdot (h \cdot c / \lambda)} \cdot A \tag{2}$$

where $P$ is the optical output power of the laser (W), $f$ is the repetition rate of the laser pulses (Hz), $hc/\lambda$ is the photon energy (J) and $A$ is the attenuation factor (unitless).

Hence, from equation (2) it is to notice that when a reference analogue detector is used, the average optical power of the QKD source must be measured at single photon levels. However, since it is currently not available, the attenuators must be calibrated with a laser at high power levels using a standard detector (InGaAs-Photodiode).

The photon distribution of a QKD source implies to determine its photon statistic. This can be measured directly by using a photon-number-resolving(PNR)transition-edge sensors(TESs) [3].

### ***Experimental implementation***

#### **Mean photon number**

Figure 1 shows the setup to measure the mean photon number of a QKD laser source consisting of a strong attenuated pulsed laser source. When a reference analogue detector is used, the laser source has to be pulsed at high repetition rate, or low attenuation, to generate enough optical power that can be measured with a reference analogue detector. By knowing the attenuator transmission the mean photon number can be calculated using equation (2). If the measurement system were sensible to the pulse shape of the laser source, the laser source pulse shape must be characterized at different repetiton rates from where a correction factor must be determined. In figure 2, the characterisation of a laser source operated at different repetition rates is shown, where a change of the pulse shape is observed.

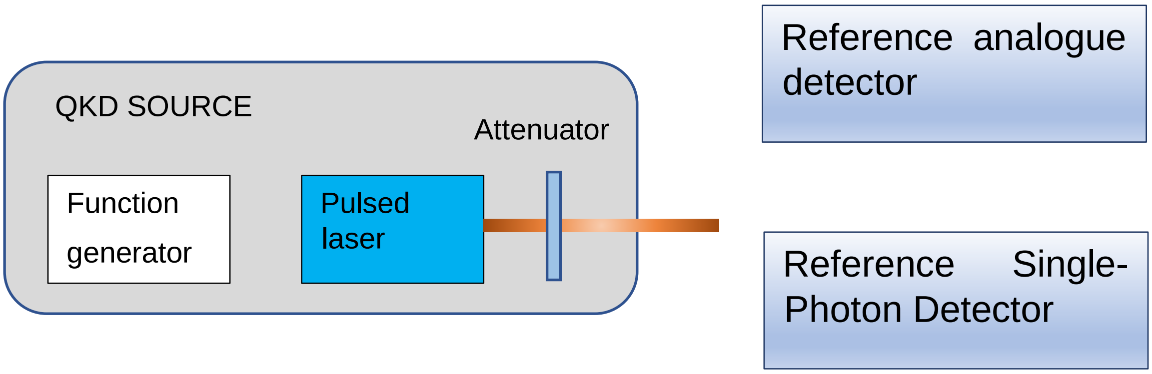


*Figure 1: Experimental implementation scheme of the facility for determining the mean photon number of a QKD laser source using a reference analogue detector or a single-photon detector.*

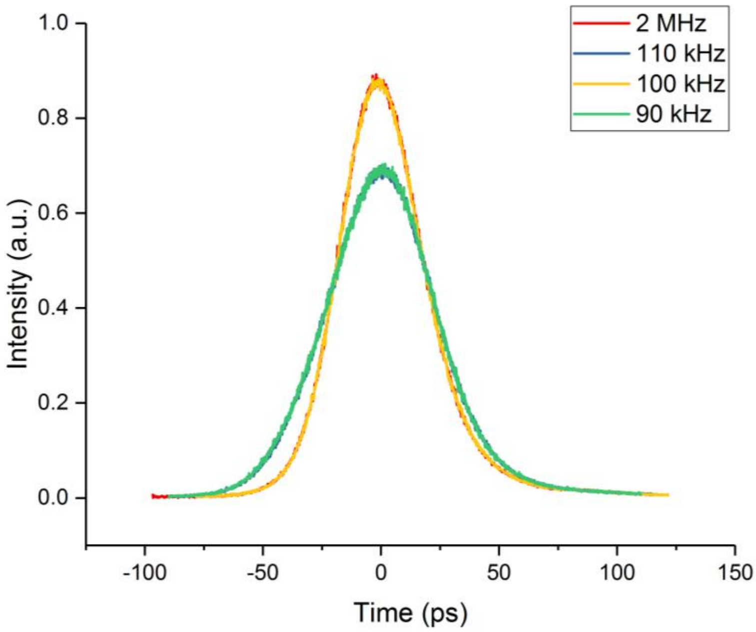


*Figure 2. Pulse shapes from ID300 pulsed laser at varying repetition rates measured with an Agilent Infiniium DCA-J 86100C digital sampling oscilloscope with Agilent 86116B 65 GHz optical head.*

**Photon distribution**

The photon distribution of QKD source can be directly determined by using a Photon-Number-Resolving Transition-Edge Sensor (TES detector). Figure 3 shows a stand-alone measurement system with two fiber-coupled TESs integrated within a compact adiabatic demagnetization refrigerator (ADR) developed at the TUB for this purpose. As an example, the photon distribution of two different light sources (e.g. incandescent lamp and laser) is shown in figure 3 (Right). Here the thermal and Poisson distribution are clearly observed.

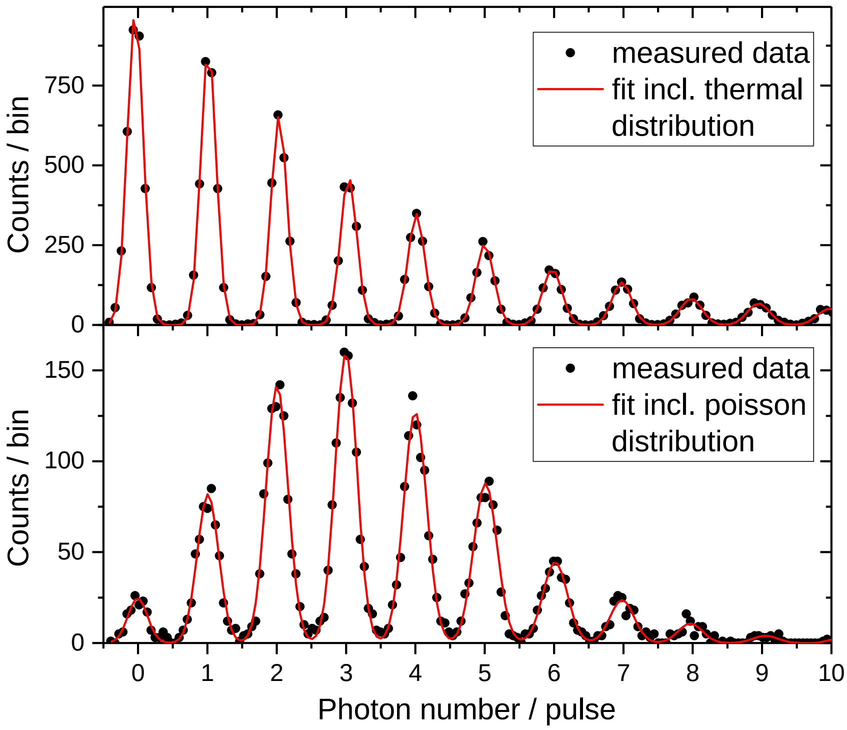


*Figure 3: Left: TES Detector developed at the Technical University of Berlin (TUB). Right: Photon distribution of a thermal and laser source measured with the TEST detector.*

## ***References***


[1] Z. L. Yuan, J. Y. Cheung, T. Debuisschert, I. P. Degiovanni, J.-M. Merolla, A. Poppe, A. J. Shields, and A. G. Sinclair, "Quantum Key Distribution; Components and Internal Interfaces," (European Telecommunications Standards Institute (ETSI), 2010).

[2] Alan Migdall, Sergey V. Polyakov, Jingyun Fan and Joshua C. Bienfang, “Single-photon generation and detection”, Volume 45, Academic Press, 2013

[3] M. Schmidt, M. von Helversen, M. López, F. Gericke, E. Schlottmann, T. Heindel, S. Kück, S. Reitzenstein, J. Beyer, Photon-Number-Resolving Transition-Edge Sensors for the Metrology of Quantum Light Source, J Low Temp Phys https://doi.org/10.1007/s10909-018-1932-1

## *How to build a high-resolution single-photon spectrometer suitable for free-space QKD applications?*

*The description of the design and performance will be included in a future update after publication in the open literature.*

# *How to characterise the spatial modes of emitted/transmitted photons of a single photon source, exploiting different kinds of spatially resolving detectors (e.g. EMCCD, SPAD Array)?*

## ***Introduction***

The characterization of the spatial mode of a single photon source can be done measuring the far field of the source with a spatial resolving detector. The detector, if operated correctly as described below, will directly provide a faithful representation of the whole spatial distribution $P(x)$ (normalized to the unity) i.e. a matrix in which each pixel value represents $P_{click}(x) = N_{ph}P(x)\eta(x)$ , where $N_{Ph}$ is the photon emitted by the source and $\eta(x)$ is the quantum efficiency of the pixel at the coordinates $x =$ (x, y). From that distribution, some parameter such as the centre (the spatial mean value) and the width (the spatial standard deviation) can be evaluate. *The model described in A 2.2.5 allows to predict an uncertainty on the estimation of the centre of the distribution.*

## ***SPAD array***

SPAD array are constituted by a matrix of independent SPADs each with its read-out electronics. They are fast, even if not as fast as a single SPAD due to the bottleneck of the read out of big amount of data, and have a low noise level, comparable with the one of a single SPAD (50-100 counts per pixel per second). The net efficiency is also smaller than the stand-alone device because of the small fill factor. With the use of micro-lenses for coupling the light it is around $\eta$ = 20% at the peak. The resolution is lower than other spatially resolving devices, such as CCD camera.

**Procedure for measuring a spatial profile**

1. To perform a set of measurements (frames) without light in order to evaluate the probability of a noise count per pixel par frame $P_{noise}$ . In general, $P_{noise}$ will be proportional the acquisition time of the frame. It is important to work in the linear regime, far from saturation, i.e. to set the time window so that $P_{noise}$<<1.
2. SPADs array *often present outliers*, i.e. pixels which a $P_{noise}$ much larger than the average, and this can distort the representation of the spatial profile and the estimation of the parameters of the distribution. Thus, it is fundamental to apply a correction algorithm. Some of these outliers are "hot" pixels easily to be recognized, but there are spikes that appear randomly distributed from one image to the other ("warm" pixels). Therefore, a properly designed smoothing algorithm removing strong discontinuities in the images must be developed, usually based on a smoothing procedure.
3. The uniformity of the response of the array $\eta(x) = \eta$ should be tested and corrected.
4. After the noise level is evaluated, one needs to adjust the photon rate of the source and the acquisition time of the single frame so that *the detector is operated far from saturation*. The probability of a photon detection per pixel per frame should be much less than one, namely $P_{click}(x) < 0.1$.
5. The evaluation of the spatial profile can be obtained summing up many frames, in order to have a statistically significant number of count per pixel in the final image. The true counts distribution can be estimated by $\hat{P}_{click}(x) = \frac{N_{click}(x)}{N_{frame}} - P_{noise}$. It is important to subtract the mean value of the background counts in order to avoid bias in the estimation of the parameters of the distribution.
6. The coordinates of the centre of mass of the distribution can be obtained by

$$\hat{\mathrm{x}} = \left(\frac{1}{N_{tot}}\right)\sum_{i=1}^{N_{pix}^{(\mathrm{x})}} \mathrm{x}_i \, N_{click}(\mathrm{x}_i) \tag{1}$$

   with $N_{click}(\mathrm{x}_i) = \sum_{j=1}^{N_{pix}^{(\mathrm{y})}} N_{click}\left(\mathrm{x}_i \, , \mathrm{y}_j\right)$ the marginal counts distribution along x-coordinate. Analog expression holds for the y-coordinate.

7. Assuming a Poissonian distribution of the true counts for each pixel, perfectly compatible with the assumption above, the uncertainty on the estimation of the position of the center of the spatial mode turns out to be (in terms of number of pixels):

$$\Delta^2\hat{\mathrm{x}} = \left(\frac{1}{N_{tot}}\right)\left[\widehat{\sigma_{\mathrm{x}}} + K_{\mathrm{x}}\,(\Delta^2 P_{noise}\,N_{pix})/(\eta\,N_{Ph})\right] \tag{2}$$

$\Delta^2 P_{noise}$ = the variance of the noise counts per pixel per frame
$\widehat{\sigma_{\mathrm{x}}}$ = the variance of the spatial distribution of the true counts (estimated)

This equation states clearly the role of the quantum efficiency and the fluctuation of the noise floor, anyway one can set the adjustable parameter, in particular the total number of photon detected $N_{tot} = N_{frame}\,N_{Ph}\eta$ in order to arbitrarily decrease this uncertainty. Of course, it could require longer measurement, so that a good compromise can be obtained for example requiring that $\Delta\hat{\mathrm{x}} \leq 1$ pix, thus matching or surpassing the resolution of the detector.

Note that, in the Eq. (2), the quantity $K_{\mathrm{x}} = \sum_i\ (\mathrm{x}_i - \hat{\mathrm{x}})^2/N_{pix}^{(\mathrm{x})}$ represents the mean square of the pixels distance from the center of the spatial mode. This term is larger if the center of the spatial distribution is not kept at the geometric center of the pixel matrix. This is due to the fact that a random noise count appearing on one side of the peak has some chance to be compensated by another appearing in the other side, if the peak is centred. If the peak of the true counts is close to a border of the array, most of the noise counts will appear on the same side of the peak, introducing a random bias in the determination of the centre. Therefore, we strongly suggest working with the spatial mode well centred in the sensor. Of course, this condition can be verified a posteriori end eventually corrected in a reiterative process.

**EMCCD**

These devices have got an high resolution (the order of a megapixels for scientific cameras), a quantum efficiency that can be as high as $\eta_0 = 95\%$ in the visible. The speed of the detector depends on the number of pixels of the image (it can be freely set), since the pixel are read out sequentially at the maximum rate of few tens of MHz. On the other side, they have an digitalization electronic read noise (following a Gaussian distribution) with a standard deviation of few tens of counts per pixel in the MHz read out rate. In the electron multiplying regime, the read noise is made negligible with respect to the electronic signal generated by an absorbed photon and a subsequent electron avalanche. This fact restores the sensitivity to the single photon. However, the multiplying register induces the generation of spurious charge (“clock induced charge”) with a probability $p_{spc}$ of some part in$10^{-3}$ per pixel per frame that experience multiplying process too and are hardly distinguishable from the signal of a true photon. The “on–off” behavior is achieved by applying a discriminating threshold $T$ on the electron counts $n_e$ at each pixel: a photon is detected if $n_e$ > T. At the increasing of $T$ the probability of detecting a false signal $P_{noise}(T)$ due to the tails of the electronic read noise or a spurious pulse decreases, at the expense of reducing the probability of detecting the pulse due to a photon, therefore lowering the effective quantum efficiency $\eta(T)$. Thus, in order to properly operate this device as single photon detector’s array, the following procedure should be used for estimating the parameter of the device and setting the threshold:

3. It is important to set a high electron multiplying gain level $g$ in order to reduce the effect of the read noise. Typically, in the top-level models, this gain can be set to $g = 1000$.
4. Figure 1(a) presents a typical histogram of the electron count distribution per pixel for a frame acquired without light, showing excellent agreement between the experimental data and the theoretical prediction of the model developed in [1]. Two different behaviours are clearly visible: at low-count levels, the Gaussian contribution of read noise is dominant; at high-count levels, only the exponential contribution of spurious charges is observable. By fitting the with the first part of the histogram with a Gaussian distribution, on one can estimate the mean value $\hat{x}_{RN}$ and the standard deviation $\sigma_{RN}$ of the read noise. By fitting the distribution of spurious charge on the second part of the histogram with the function $p_{spc}\ ({g_{spc}}^{-1} e^{-x/g_{spc}})$ (see [1]), one obtains the probability of a spurious event $p_{spc}$ and the multiplying gain $g_{spc}$.
   Similarly, an acquisition of a frame in presence of light generate a histogram like the one of Figure 1(b). Even in this case, the fitting of the exponential part by the function $p_{ph}\ ({g_{ph}}^{-1} e^{-x/g_{ph}})$, once the probability distribution of the spurious counts previously estimated has been subtracted, allows to estimate the photon detection probability per pixel per frame $p_{ph}$. *The light intensity must be selected to avoid double events and to guarantee that spurious charges are negligible with respect to*

*photoelectrons i.e.* $p_{spc} \ll p_{ph} \ll 1$ . Since $p_{spc}$ is usually of few part in $10^{-3}$, a convenient value for the photon detection event is $p_{ph} \sim 0.1$ per pixel per frame.

5. The final step is to establish the threshold $T$. It can be done conveniently by setting $T > \hat{x}_{RN} + 3\sigma_{RN}$ , to exclude the read noise. Of course, aside the read noise suppression, the increasing of the threshold reduces the probability of a noise count $P_{noise}(T)$ but also the effective efficiency in detecting true photon $\eta(T)$. The dependence of the efficiency from the threshold depends on the specific parameter according to the model developed in [1]. However one can expect, with the parameters of the top-level camera on the market to have a $P_{noise}(T = \hat{x}_{RN} + 3\sigma_{RN}) \approx 2 \times 10^{-3}$ and an efficiency of $\eta(T = \hat{x}_{RN} + 3\sigma_{RN}) \sim 0.5\,\eta_0$, where $\eta_0$ is the efficiency measured in the linear regime.

After the preliminary characterization of the EMCCD camera has been performed, the same procedure and measurement guide lines described in the SPAD array section "Procedure for measuring a spatial profile", points 1-3-4-5-6-7 should be carried out.

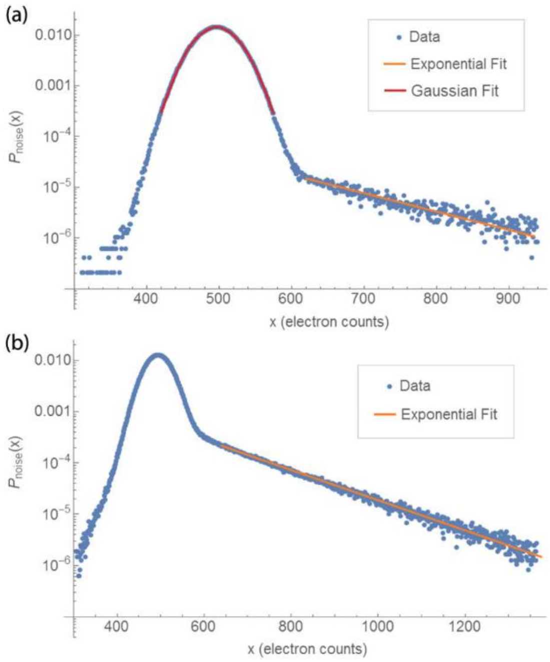


*Figure 1: Logarithmic scale histogram of the electron counts distribution for a frame acquired without incident light (a) and with incident light (b). Gaussian curve fit (red line). Exponential curve fit (orange line).*

## ***References***

[1] A. Avella, et al., "Absolute calibration of an EMCCD camera by quantum correlation, linking photon counting to the analog regime", Optics Letter 41, No. 8 (2016).

## *How to characterize the single-photon sources developed in within this project with respect to photon out-coupling efficiency, quantum nature in terms of the $g^{(2)}(0)$-value, emission spectra?*

### ***Photon out-coupling efficiency***

When considering the efficiency with which one collects single photons out of a single quantum emitter it is useful to break the total experimental system down into several distinct levels, each of which may be responsible for particular reductions in efficiency.

Here, the total efficiency is considered to be a product of the system efficiency ($\eta_{sys}$) the photon out-coupling efficiency ($\eta_{oc}$) and the internal quantum efficiency ($\eta_{iqe}$), as depicted in Figure 1. These factors account for photon losses in the macroscopic optical system including detector efficiency, the near-field optical structures and the efficiency of the quantum system itself.

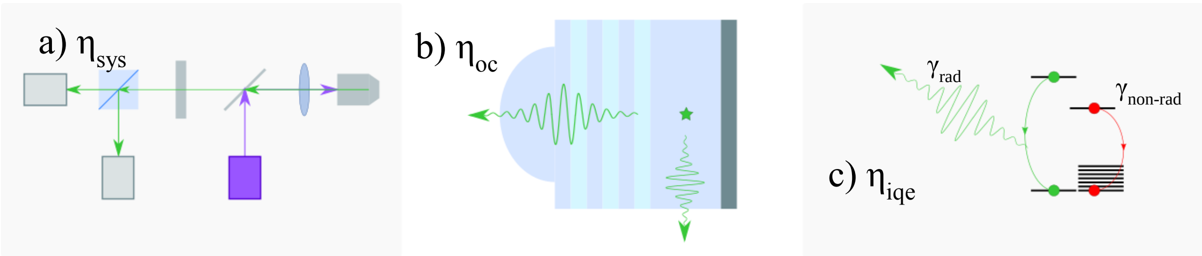


*Figure 2: Pictorial depiction of:*
*a) System efficiency, comprised of the external optics and detectors.*
*b) Out-coupling efficiency determined by the efficacy of any optical micro-structures or nano-structures employed.*
*c) The internal quantum efficiency of the quantum system producing photons. This depends on the alternative decay routes available to the optical transition, as well as other charge states which may exist for the system.*

The photon out-coupling efficiency defines the fraction of light generated within a device that is coupled to the outside world, and therefore available for use. The external quantum efficiency of a light emitter is the product of the internal quantum efficiency and the photon out-coupling efficiency.

The total efficiency can be most directly ascertained via pulsed saturation intensity measurements. Upon reaching the saturation power for a pulsed excitation scheme the total system efficiency can be straightforwardly found from the excitation rate and the collected emission rate. The transmission of the optical set-up can be characterised a priori, for example by illuminating a pin-hole with a laser at the emission wavelength to simulate the quantum emitter, which provides a value for the system efficiency ($\eta_{sys}$). The optical transmittance component of $\eta_{sys}$ should be in the 10% regime for a well-designed system.

It is significantly harder to decouple the internal quantum efficiency and the out-coupling efficiency for individual optically addressed emitters. For weakly-coupled micro-optical / quantum systems, phenomena such as the Purcell effect, which is affected by the microstructure, can alter the quantum efficiency through excited state lifetime changes. For the strongly-coupled case it is fundamentally impossible to extricate the two systems.

Finite difference time domain (FDTD) and finite element (FE) simulations can provide estimates for the out-coupling efficiency, but are often only accurate in the ideal case. Time-resolved photo-luminescence (TRPL) provides the total decay rate ($\gamma_{tot}$) which is the sum of the non-radiative and radiative rates ($\gamma_{rad}$ + $\gamma_{non\text{-}rad}$), but falls short of a direct value for $\eta_{qe}$ since this is found by dividing the radiative rate by the total rate ($\gamma_{rad}$ / $\gamma_{tot}$). Implementation of Drexhage's scheme [1] can give direct experimental values for the quantum efficiency by varying the local density of states. It is the combined effect of both out-coupling and quantum efficiencies which is the most relevant figure of merit for a single-photon source, so an inability to distinguish between these two factors may not be absolutely necessary. One important factor when considering the efficiency of a single-photon source is the number of spatial modes that are populated. Most realistic technological implementations of a single-photon source involve coupling to a single-mode fibre at some stage. Therefore, if many spatially orthogonal modes are mapped onto the active area of a single-photon detector, it is possible that a higher flux of photons (i.e. a higher efficiency) may be quoted than would be usefully realised in a deployable system.

## ***Second order correlation function, $g^{(2)}(0)$***

The most important evaluation of a single-photon source is to measure the probability of more than one photon being emitted by the source within a prescribed time interval. The parameter normally employed to characterise this property of an SPS is the second order correlation function (or Glauber function) defined as

$$g^{(2)}(\tau = 0) = \left[\frac{\langle I(t)\, I(t+\tau)\rangle}{\langle I(t)\rangle\langle I(t+\tau)\rangle}\right]_{\tau=0} \tag{1}$$

where *I*(t) is the intensity of the optical field. In the low photon flux regime, this parameter has been shown to be substantially equivalent to the $\alpha$ parameter introduced by Grangier et al. [2], which is experimentally measured as the ratio between the coincidence probability at the output of a Hanbury Brown and Twiss interferometer (HBT) [3, 4], typically implemented by a 50:50 beam-splitter connected to two non-photon-number-resolving detectors, and the product of the click probabilities at the two detectors, i. e:

$$g^{(2)}(\tau = 0) \approx \alpha = \frac{P_c}{P_r P_t} \tag{2}$$

where $P_c$, $P_r$, $P_t$ are, respectively, the coincidence probability and the click probabilities at the reflection and transmission outputs ports of an HBT.

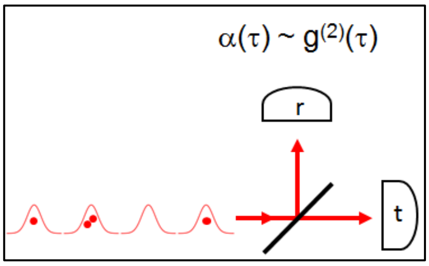


*Figure 2. Schematic of a Hanbury Brown – Twiss interferometer, ideally comprising a 50:50 beamsplitter and single-photon detectors at the r(eflection) and t(ransmission) output ports.*

Due to the equivalence between $g^{(2)}(0)$ and $\alpha$ in the regime typical of quantum optics experiments, all experimental measurements of $g^{(2)}(0)$ in the relevant literature are actually measurements of $\alpha$, since the two parameters are used substantially without distinction in this community.

Probabilities $P_c$, $P_r$, $P_t$ are estimated as the ratio between the total number of the corresponding events versus the number of excitation pulses during the experiment. The value of the measurand is independent from the total efficiencies ($\eta_r$, $\eta_t$) of individual channels (including detection and coupling efficiency), optical losses and splitting ratio since

$$\alpha = \frac{\eta_r \eta_t P_c}{\eta_r P_r \eta_t P_t} = \frac{P_c}{P_r P_t} \tag{3}$$

The value of the parameter from the experimental data, corrected for the contribution of the background coincidences (due, for example, to stray light or residual excitation light), can be estimated as follows:

$$\alpha = \frac{P_c - P_{cbg}}{(P_r - P_{rbg})(P_t - P_{tbg})} \tag{4}$$

where $P_{cbg}$, $P_{rbg}$, $P_{tbg}$ are, respectively, the coincidence and click probabilities of background photons, calculated analogously to their counterparts $P_c$, $P_r$, $P_t$.

The HBT can be constructed from free-space or fibre-coupled components. Two key parameters are the jitter of the detectors and recording electronics, and the presence of backflash. Jitter will smear out the $g^{(2)}(\tau)$ curve, while backflash can lead to spurious signals. The ideal is to use the lowest-jitter detectors and electronics. Where this is not feasible, then corrections to the $g^{(2)}(\tau)$ curve shall be performed. Backflash is caused by emission from the detection event being propagated out from the detector and being detected by the same or other detector after reflections in the optical path. Since backflash emission is at a longer wavelength than the single-photon emission being measured, spectral filtering can be used to remove it. With fibre-coupled HBTs, extra lengths of fibre can be used to move the backflash away from the $\tau$=0 region of the $g^{(2)}(\tau)$ curve.

The value of $g^2(0)$ should reach a value of 0 for a perfect single-photon source. A value below 0.5 cannot be explained by classical wave mechanics, and so it is taken as an upper limit of the visibility of this quantum phenomenon.

The figure below gives one example of a multi-HBT set-up, used in a recent comparison of $g^{(2)}(\tau)$ measurements [4].

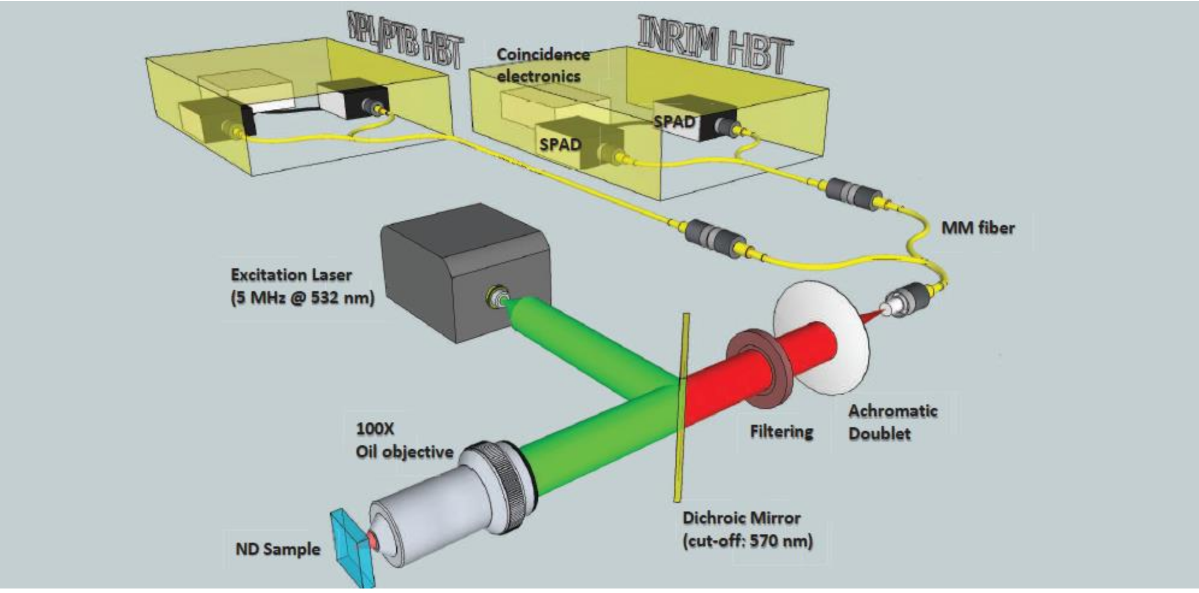


*Figure 3. Scheme of the experimental setup: the output of a laser-scanning confocal microscope is split by a 50:50 fibre beam-splitter and directed to two independent HBT measurement systems for performing the comparison. One of the HBTs is held by the host institution (INRIM) while the other one is provided, in turn, by the other two partners (NPL, PTB)*

## ***Emission spectra***

Spectral characterisation provides essential information about quantum photonic sources. It can be used to isolate and identify single quantum emitters, or assess the suitability of a source for a specific application. Grating spectrometers with electron-multiplying charged coupled devices can be used to record spectra at the single-photon level across a wide range of wavelengths, but do not always provide the high resolution and low loss required to investigate individual quantum emitters. The scanning Fabry-Perot interferometer (SFPI) provides superior resolution at a cost of limited scan range. It involves coupling light into a tuneable optical cavity, scanning its resonant frequency and measuring the transmitted intensity. In both cases, the photodetector is selected to match the required spectral range of the measurements.

The main factors that differentiate the two approaches are spectral range and resolution. In grating spectrometers, the maximum spectral range that can be continuously characterised depends on the focal length of the spectrometer, the line density of the grating and the size of the detector's active area. The spectral resolution of grating spectrometers also depends on focal length and line density, and on the size of the individual pixels in the detector at the focal plane. While spectral range is not generally a limiting factor, a number of experiments have reported resolution-limited linewidths in photonic source characterisation with grating spectrometers.

The SFPI is almost opposite in its attributes; the maximum scan range is limited by the free spectral range (FSR) of the cavity, which is inversely proportional to cavity length (L):

$$FSR = \frac{c}{2L} \tag{5}$$

This means that to span 10 nm about a central wavelength of 900 nm, which would be straightforward with a grating spectrometer, would require a very short cavity length of 40 μm. It is evident then that the range that can be displayed in one spectrum is a limiting factor for SFPIs. The benefit is that they can far surpass the resolution of grating spectrometers for localised spectral features; the resolution depends on the cavity linewidth, which in turn depends on the reflectivity of the mirrors. With the high-reflectivity dielectric coatings that are commercially available, resolution less than 1 picometer (~ 1.5 μeV ~0.37 GHz) have been achieved [5, 6]. An additional consideration is the duration of the measurement; while grating spectrometers can take a simultaneous snapshot of all wavelengths in the spectrum, SFPIs scan the wavelengths sequentially, which requires significantly longer.

## ***References***


[1] A. Mohtashami and A. F. Koenderink, New Journal of Physics, [15], 043017 (2013), https://doi.org/10.1088/1367-2630/15/4/043017

[2] P. Grangier, G. Roger, and A. Aspect, Europhys. Lett. 11, 173-179 (1986)

[3] R. Hanbury Brown and R. Q. Twiss, Nature (London) 177, 27 (1956)

[4] E. Moreva et al., arXiv:1807.04502

[5] R. Hafenbrak et al., New J. Phys. 9, 315 (2007).

[6] S. Ates, et al., Phys. Rev. Lett. 103, 1 (2009).

## *How to measure the lifetime, coherence time and the degree of indistinguishability of photons emitted by fibre-coupled single-photon emitters?*

### ***Spontaneous emission lifetime***

The lifetime $\tau_s$ of a single emitter will generally be a combination of the intrinsic radiation lifetime, the dephasing time, and non-radiative transitions, and can be measured by using pulsed excitation.

Exploiting time-correlated photon-counting and performing coincidence measurements between the triggering signal and the detected photon, one obtains a temporal profile corresponding to the convolution the different components of the experiment, i.e. the radiation from of the emitter, the detector, and the TCSPC instrumentation (the last is usually negligible). The ideal situation is when both TCSPC electronics as well as the single-photon detector have negligible jitter with respect to the source. When this is not the case, a proper characterisation of the detector and TCSPC electronics should be performed in order to deconvolve the profile of interest. A single-photon detector with the possible lowest jitter is needed for this measurement. Superconducting nanowire detectors, which can have a jitter of just tens of picoseconds [1] appear to be the best for this purpose.

For characterisation of single-photon sources, spectral filtering (e.g. by using a grating spectrometer) is normally used to isolate the spectral region(s) of interest. This spectral range is then sent to the photon-counting apparatus for TCSPC. The spontaneous emission lifetime can then be estimated by fitting a decaying exponential function to the TCSPC data.

### ***Coherence time***

The coherence length, and hence the coherence time $\tau_c$ can be measured using a Michelson or Mach-Zehnder interferometer to produce single-photon self-interference [2]. The coherence length is the 1/e decay point of the interference envelope, when measured in optical path difference units, and the coherence time is obtained by dividing this distance by the speed of light.

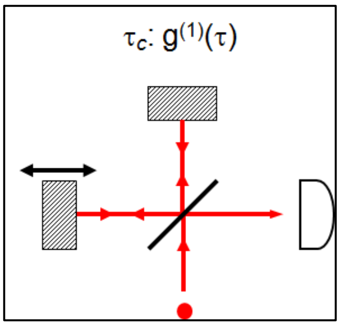


*Figure 1. Schematic of a Michelson interferometer, used for measuring single-photon interference.*

One such set-up, implemented at NPL [3], is described below.

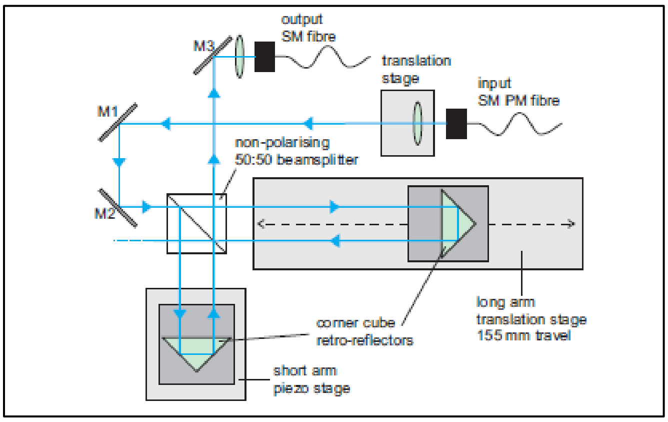


*Figure 2. Schematic of Michelson interferometer at NPL to measure coherence time.*

With the interferometer set up so that the optical path lengths are the same in each arm, moving one arm by a few wavelengths results in interference fringes at the interferometer output. The visibility of these fringes, *V*, is defined as:

$$V = \frac{I_{max} - I_{max}}{I_{max} + I_{max}} \tag{1}$$

where $I_{max}$ and $I_{min}$ are the maximum and minimum intensities of the interference fringes.

Many factors can degrade the visibility, reducing it from the maximum value of one, including misalignment of the optics, background light entering the detector and dark counts in the detector. The important part of the optical setup is to ensure that the two beams, when recombined on the beam splitter, are spatially overlapped with a high degree of accuracy.

Once an interference pattern with high visibility has been produced at zero path difference, a measure of the coherence length can be made by scanning the optical path difference between the arms over a large distance. The visibility of the interference fringes will decrease with increasing difference in path length. The coherence length is defined here as the path difference required to reduce the visibility to 1/e of its value at the zero path difference position. Highly coherent light sources such as single frequency lasers will have coherence lengths of many kilometres, however, non-coherent sources such as LEDs and quantum dots emitters will have coherence lengths of the order of millimetres, allowing measurement by bench-top apparatus.

The interferometer (figure 2) has a `short arm' and a `long arm', the short arm retroreflector could be translated over a few microns to produce interference fringes, while the long arm retroreflector could be translated over up to 155 millimetres to enable measurement of coherence lengths.

The input to the interferometer is through a polarisation maintaining (PM) fibre, single mode for the wavelengths under investigation. A zero-order half wave plate and polarising beamsplitter can be placed at the input to the fibre to ensure that the incoming photons' polarisation is rotated to match the axis of the PM fibre and that other polarisations in the beam are rejected.

The lens used to collimate the light out of the input fibre is mounted on a micrometre translation stage to obtain precise collimation.

Two mirrors (M1 & M2) steer the beam through a 50:50 non-polarising beam splitter and along the long arm. A corner cube retro-reflector was mounted on four-axis alignment stage and bolted on to the moving platform of the long arm. The short arm consisted of a similar retro-reflector mounted on an alignment stage bolted onto a piezo-actuated single-axis translation stage. The stage could be scanned accurately over a number of microns. The combined beams were coupled into a single mode fibre for routing to a single-photon detector.

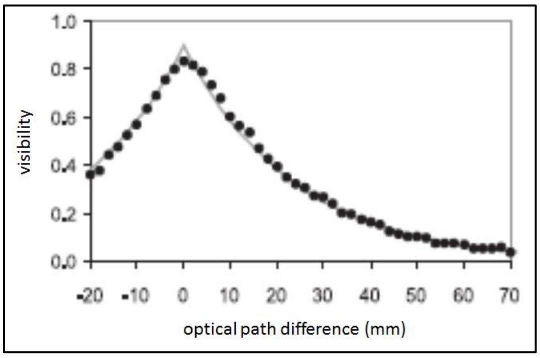


*Figure 3. Example of a measurement obtained for a quantum dot sample, yielding a coherence length of 23.6 mm.*

## ***Degree of indistinguishability***

Indistinguishability is measured using Hong-Ou-Mandel interference [4]. If two photons are perfectly indistinguishable, i.e. they are in exactly the same mode, and are each incident at the same time at the separate input ports of a 50/50 beamsplitter, they will 'bunch' or 'coalesce', i.e. both will exit together from one of the exit ports. The interference curve is usually measured by placing a photon counting detector at each output port of the beamsplitter and measuring the detection coincidences $N_c$ as the time delay $\Delta\tau$ between the photons being incident at the input ports is varied. The detection coincidences will be a minimum for zero time delay; fully destructive interference will only occur if the two photons are completely indistinguishable. The widely accepted definition for the measured HOM dip visibility is given by

$$V_{measured} = \frac{N_{c,\Delta\tau >> \Delta\tau_{dip}} - N_{c,\Delta\tau=0}}{N_{c,\Delta\tau >> \Delta\tau_{dip}}} \tag{2}$$

where $\Delta\tau_{dip}$ is the width of the interference dip, $N_{c,\Delta\tau >> \Delta\tau_{dip}}$ is the measured coincidence rate far from the dip region where the photon wavepackets overlap, and $N_{c,\Delta\tau=0}$ is the measured coincidence rate at the bottom of the dip.

Data-fitting is usually applied to the interference curve, whose form depends on the spectrum of the interfering photons [5], as well as imperfections in the experimental setup, in order to extract a reliable value for the interference visibility, and hence the indistinguishability [6].

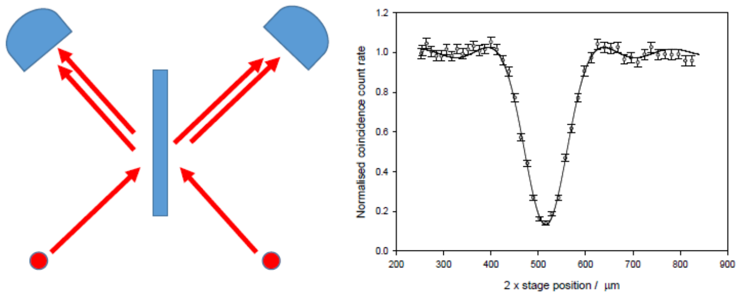


*Figure 4. Schematic of a Hong-Ou-Mandel interferometer interferometer, used for two-photon interference.*

One such set-up, implemented at TUB to study quantum dots, is described below.

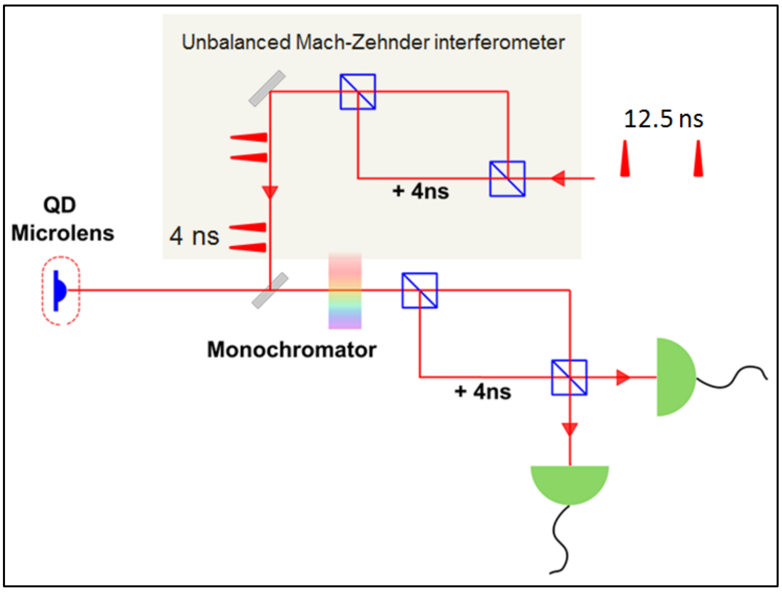


*Figure 5. Schematic of the overall experimental set-up. The AMZIs (see text) are implemented with PM fibres.*

A mode-locked Ti:sapphire laser operating in picosecond mode generates optical pulses at a repetition rate of 80 MHz. These pulses are converted to a sequence of double-pulses with pulse-separation of Δt by utilizing an asymmetric Mach-Zehnder interferometer (AMZI, grey box in figure 5). The AMZI is actually implemented with polarization maintaining (PM) single-mode fibres. By choosing different fibre-delays within one arm of the interferometer, Δt can be varied from 2.0 ns to 12.5 ns. This two-pulse sequence is then launched onto a sample via a microscope objective (MO) with a numerical aperture of 0.4. The same MO is used to collect and collimate the sample emission, which is subsequently focused onto the entrance slit of a grating monochromator with spectral resolution of 0.017 nm (25 μeV). A linear polarizer and λ/2 waveplate before the spectrometer (not shown in figure 4) allow for polarization selection of particular sample states [7].

To perform Hong-Ou-Mandel (HOM) -type two-photon interference (TPI) experiments, a second AMZI is attached to the output port of the spectrometer. Using a λ/2 waveplate, the polarization of the photons in one interferometer arm can be switched, either being co- or cross-polarized with respect to the other arm. This second AMZI is also implemented with polarisation-maintaining fibres (figure 6). In order to interfere consecutively emitted single photons at the second beam-splitter, a variable fibre delay matched to the respective pulse-separation Δt is implemented in one interferometer arm. The photon arrival time at the second beam-1splitter can be fine-tuned with a precision of 3 ps. Finally, photons are detected at the two interferometer outputs using non-photon-number-resolving silicon-based single-photon avalanche photodiodes (SPADs) and photon coincidences are recorded via time-correlated single-photon counting (TCSPC) electronics enabling coincidence measurements with an overall timing resolution of 350 ps.

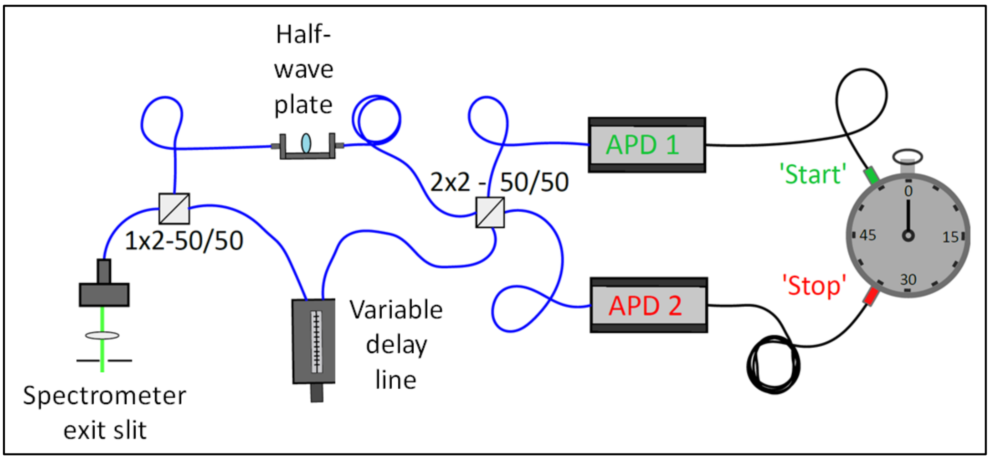


*Figure 6. Hong-Ou-Mandel two-photon interferometer implemented with polarisation-maintaining fibre.*

To extract the TPI visibilities from the coincidence histograms obtained for co-polarized measurement configuration, the peak area ratios can be considered [7, 8]. Figure 7 illustrates the coincidence pulse patterns resulting from the applied two-pulse sequences with pulse-separations Δt. The peak area ratios deduced from the probability distribution of all possible pathway combinations are represented by the respective bar height. Each pattern is composed of five-peak clusters with temporal delays of T = 12.5 ns according to the laser's fundamental repetition rate. The five-peak cluster arises from the possible pathway-combinations taken by two photons separated by Δt. Thus, the peak area ratios can easily be deduced considering combinatorics, which enables us to extract the TPI visibility quantitatively. The expected peak area ratio of each cluster is 1:4:6:4:1, except for the cluster centred at zero-delay (Δt = 0). Here, the peak area ratio depends on the photon-indistinguishability. In case of perfect indistinguishability, the coincidences at Δt = 0 vanish and the peak area ratios of the cluster becomes 1:2:0:2:1. Photons which are distinguishable, e.g. due to their polarization, lead to an area ratio of 1:2:2:2:1.

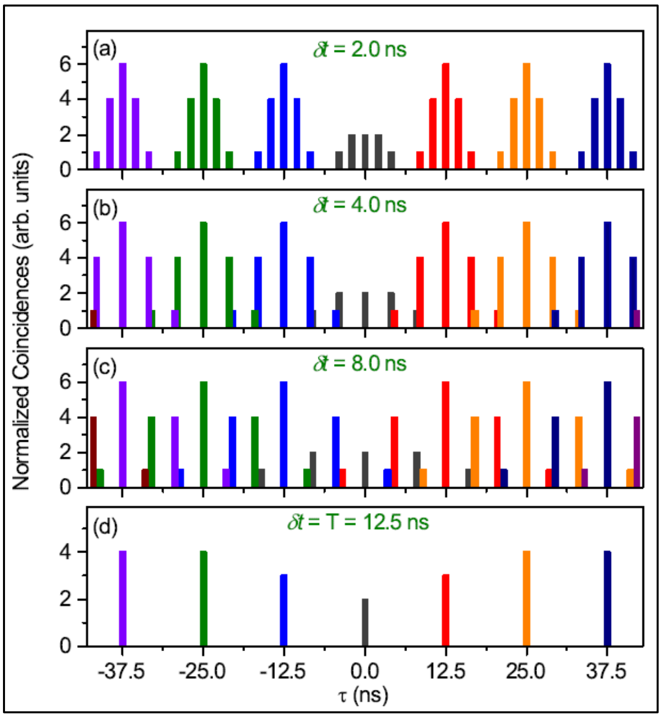


*Figure 7. Schematic coincidence pulse patterns resulting from a two-pulse sequence with a pulse-separation Δt repeating every T = 12:5 ns. The expected peak area ratios in case of distinguishable photons are encoded in the the height of each bar [8].*

The peak areas of the central cluster are labelled $A'_2$:$A'_1$:$A_0$:$A_1$:$A_2$ and <A> = ($A'_1$ + $A_1$)/2.

The TPI visibility for Δt = 2, 4 and 8 ns is then given by

$$V = \frac{\langle A\rangle - A_0}{\langle A\rangle} = 1 - \frac{A_0}{\langle A\rangle} \tag{3}$$

In case of Δt = 4 and 8 ns, peaks $A_1$ and $A_1'$ overlap with the adjacent cluster. Hence, the visibility is given by

$$V = \frac{2\langle B\rangle/3 - A_0}{2\langle B\rangle/3} = 1 - \frac{A_0}{2\langle B\rangle/3} \tag{4}$$

where <B> is the mean value of $A_1$ and $A_1'$ and their related overlapping peaks. In case of Δt = 4 ns, $A_1$ and $A_1'$ overlap with the nearest neighbour cluster B2 and B′2. For Δt = 8 ns, the overlapping peaks stem from $C_2$ and $C_2'$. To reduce the statistical error of <A> and <B>, instead of taking only $A_1$, $A_1'$ and their overlapping peak areas into account, one can average over the peak areas for all clusters at $\tau \neq 0$, to infer a more precise normalization of the data. For the pulse separation Δt = T = 12.5 ns, the visibility is determined by

$$V = \frac{\langle A\rangle_S/2 - A_0}{\langle A\rangle_S/2} = 1 - \frac{A_0}{\langle A\rangle_S/2} \tag{5}$$

where $A_0$ is the area of the peak at $\tau = 0$ and $\langle A\rangle_S$ corresponds to the mean value of the side peaks with $|\tau| >$ 12.5 ns.

## ***References***

[1] E. A. Dauler et al., Optical Engineering 53(8), 081907 (2014)

[2] F. Jelezko, A. Volkmer, I. Popa, K. K. Rebane, and J. Wrachtrup, "Coherence length of photons from a single quantum system," Physical Review A 67(4), 041802 (2003).

[3] R A Hubbard, Ph.D. Thesis, Imperial College London (2008)

[4] C. K. Hong, Z. Y. Ou, and L. Mandel, Phys. Rev. Lett. 59(18), 2044-2046 (1987).

[5] Y.-H. Kim, J. Opt. Soc. Am. B 20(9), 1959-1966 (2003).

[6] P. J. Thomas, J. Y. Cheung, C. J. Chunnilall, and M. H. Dunn, Appl. Opt. 49(11), 2173-2182 (2010).

[7] A. Thoma, P. Schnauber, M. Gschrey, M. Seifried, J. Wolters, J. H. Schulze, A. Strittmatter, S. Rodt, A. Carmele, A. Knorr, T. Heindel, and S. Reitzenstein, Phys. Rev. Lett. 116, 033601 (2016).

[8] M. Müller, S. Bounouar, K. D. Jöns, M. Glässl, and P. Michler, Nature Photon. 8, 224 (2014).

# Measurement facilities for components used in free-space QKD

## *How to characterize systems for polarisation control (based on plates and/or Pockell's cells) used in free-space QKD systems with respect to degree of polarization?*

### ***Introduction***

In free-space QKD information is usually encoded in the polarization of photons. Polarization state is a two-level quantum system serving as bits, called "qubits". The photons are easy to be manipulated and significantly insensitive to decoherence. Nevertheless, they can suffer changes due to imperfections of the transmitting medium (quantum channel) and apparatus. Due to this fact, there exists a need for highly precise characterization of the encoded states. This characterization can be performed by setting-up a polarimeter operating at single-photon level.

### ***Single-photon Polarimeter***

The single-photon polarimeter is a measurement system that is able to perform linear and circular projection measurements on the incoming identically prepared single-photon state. This can be realized either randomly splitting the incoming photons towards a set of fixed projectors (based on polarizing-beam-splitter, quarter- and half-wave plates and single-photon detectors), or developing a system based on a polarizing-beam-splitter, single-photon detectors and, a quarter- and a half-wave plate mounted on piezo-controlled rotators to realize precise state projections.

**Procedure for characterizing polarization state**

The polarimeter is used to perform a "complete set" of state projections. "Complete set" means that these projection measurements contain the whole information necessary to reconstruct the polarization state. This reconstruction process typically exploits inversion or optimization algorithms (such as e.g. maximum likelihood, least squares, …), and it is often referred to as Quantum State Tomography [1, 2].

It is possible to describe any single qubit density matrix using the four parameters $S_0, S_1, S_2, S_3$, often refereed to (improperly) as Stokes parameters. These parameters are related to density matrix with the formula:

$$\hat{\rho} = \frac{1}{2}\sum_{i=0}^{3} S_\mathrm{i}\, \widehat{\sigma_\iota} \tag{1}$$

Where $\sigma_i$ are the Pauli spin operators plus the identity operator:

$$\widehat{\sigma_0} = \mathbf{1} = \frac{1}{2}\begin{pmatrix}1 & 0\\ 0 & 1\end{pmatrix},\ \widehat{\sigma_1} = \frac{1}{2}\begin{pmatrix}0 & 1\\ 1 & 0\end{pmatrix}, \widehat{\sigma_2} = \frac{1}{2}\begin{pmatrix}0 & i\\ -i & 0\end{pmatrix}, \widehat{\sigma_3} = \frac{1}{2}\begin{pmatrix}1 & 0\\ 0 & -1\end{pmatrix} \tag{2}$$

and $S_0 = 1$. (3)

The quantum polarization states can be mapped as points on the Poincare Sphere, and the Stokes parameters $\{S_1, S_2, S_3\}$ are the coordinates on the sphere (fig. 1).

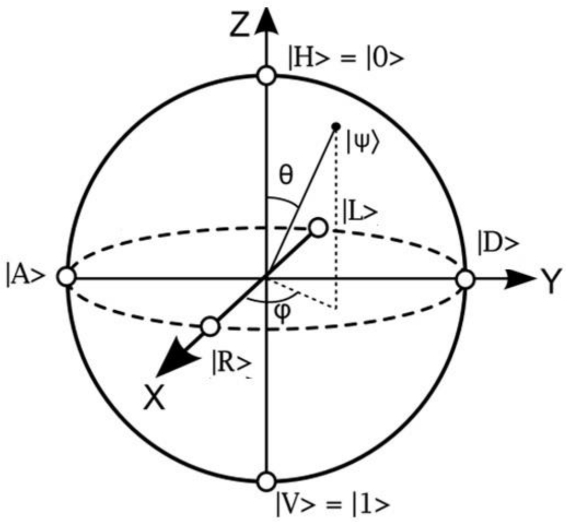


*Figure 1: Example of state represented on Poincare Sphere*

Quantum State Tomography, as an example, can be obtained by projecting a generic state $|\Psi>$ over |H>, |D> and |R> (horizontal, diagonal, and right circular polarization). To determine the Stokes parameters, the probability of projecting a state $\hat{\rho}$ into the state $|\Phi>$ is given by formula:

$$p_{|\Phi>} = <\Phi|\,\hat{\rho}|\Phi> \tag{4}$$

Thus, we obtain the following relation with the Stokes parameters:

$$S_1 \equiv 2\,p_{|\mathrm{D}>} - 1 \tag{5a}$$

$$S_2 \equiv 2\,p_{|\mathrm{R}>} - 1 \tag{5b}$$

$$S_3 \equiv 2\,p_{|\mathrm{H}>} - 1. \tag{5c}$$

Physical density matrices are positive semidefinite, and satisfy the condition $0 < Tr\{\hat{\rho}^{\,2}\} < 1$. This condition is often violated in direct inversion (as in the equations above), because of the statistical fluctuations of photon counts and experimental inaccuracies. For this reason, it is necessary to apply optimization algorithms to find the physical density matrix that, with higher likelihood, have produced those experimental data.

## ***Reference***

[1] D. F. V. James, P. G. Kwiat, W. J. Munro and A. G. White, Measurement of qubits, Phys. Rev. A 64, 052312 (2001).

[2] Z. Hradil, J. Řeháček, J. Fiurášek, M. Ježek, Chapter 3: Maximum-Likelihood Methods in Quantum Mechanics; In: M. Paris, J. Řeháček (eds), Quantum State Estimation. Lecture Notes in Physics, vol. 649 (2004, Springer, Berlin, Heidelberg, DE).

## *How to characterize intensity modulators used in free-space QKD systems with respect to modulation depth?*

### ***Introduction***

High-speed electro-optical (EO) intensity modulated (IM) transmissions in actual free-space 'practical' QKD systems [1] are typically operated by laser sources at a constant optical output power and externally modulating the optical signal. The most common devices used for this purpose are waveguide Mach-Zehnder (MZ) modulators (typically in LiNbO3), operating as interferometric devices and exhibiting a sine transfer function: an input waveguide is split into two paths that are then recombined into an output waveguide; the two paths make up the two arms of the interferometer and the optical index modulation induced on each of them creates the intensity modulation at the output of the device. An analogue electrical signal is used to linearly modulate the optical carrier. When the optical waves over the two paths arrive in phase, they are recombined and the whole radiation exits deterministically from one of the two ports of the MZ interferometer. In the opposite case (mismatch in phases), the optical wave exits from the other port of the MZ. On the consequence of this, the IM device is able to produce a transmission loss dependent on the electrical modulation of the signal. It is important to note that a fundamental role is played by polarization, because the transmission losses are polarization dependent.
This kind of IM offers multiple benefits for the modulation of light as high modulation speed capabilities (several tens of GHz), short transition times, absence of chirp, compactness, reliability, and environmental robustness. Despite the fact that these devices have been widely used in the telecom communications, they are now a reliable resource also in the NIR spectrum, beyond that in an increasing number of photonics applications.
In order to characterise the performances of high-speed EO modulators used in free-space QKD (typically operating in the VIS-NIR spectrum; in the context of MIQC2 project the selected wavelength for transmission characterization has been selected by the consortium at 852nm), modulation-frequency-domain measurements are in general implemented to evaluate the modulation transfer function, the modulation signal analysis and the intensity noise [2]. Intensity modulators are typically described by an input voltage versus output power relationship.

### ***Characterization of MZ modulators***

In this best practice guide we consider and describe the characterization of MZ modulators with respect to modulation depth, performed with an E/O measurement consisting in a RF electrical signal applied to the modulator and a consequent measurement of the resulting output optical power response (Figure 1).

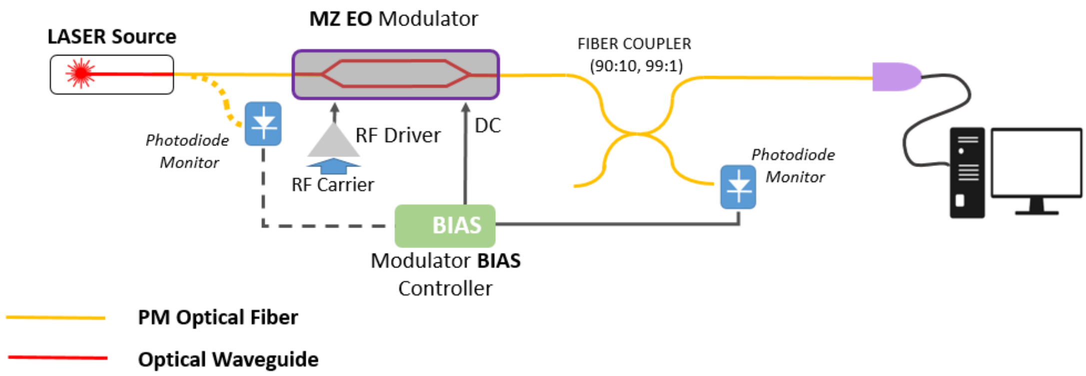


*Figure 1: Set-up scheme for EO Modulator characterization the modulation (MZ EO: Mach Zehnder Electro-Optical Modulator; RF: Radio Frequency modulation Voltage; DC: Bias Voltage). At the output of the MZ a fibre coupler with a suitable splitting ratio is inserted in order to both serve the Modulator BIAS controller and to perform measurements (with a calibrated Power meter, Oscilloscope or Lightwave component analyser).*

The recommendations, based on the experiments carried on in MIQC2 project for implementing an experimental set-up (as reported in Figure 1) for characterization are described in the following.

In stable environmental conditions, a high-stable single-frequency distributed-feedback semiconductor laser is connected to the intensity modulator by polarization maintaining fibre. The laser source optical power and modulator output optical power are measured with a calibrated power meter (insensitive with respect to optical polarization) and compared. Although the highly stable components used in MZ IM devices, due to various factors as material inhomogeneity and manufacturing tolerances, the modulator operating point (*i.e.* the point on the transfer curve around which the modulation signal is applied) can suffer slow drift due to variations of external conditions resulting in variations of the extinction ratio.

In order to optimise the operating point of MZ modulators independently from the high frequency modulation signal applied, they are designed with two sets of electrodes: 1) the RF Electrodes used to apply the RF signal; 2) the DC Bias Electrodes used to adjust with a fixed voltage the working point of the modulator.

The Bias voltage can be supplied by a simple voltage source and manually adjusted so as the desired operating point is reached. In such conditions, the voltage will have to be readjusted manually in case of drift of the modulator. It is anyway preferable the implementation of a continuously tunable bias controller (as reported in the set-up of Figure 1) to allow operation of the controlled intensity modulator at any point of its transfer function. An electronic feedback loop delivers a bias voltage to compensate any phase drift of the MZM. It maintains the working point on the modulator transfer function at a fixed position (-π/2 Phase shift) minimizing 2nd harmonic distortions.

Once the operating point is selected, and the proper bias voltage applied, one can apply the modulation signal to the modulation electrodes. The typical switching voltage $V\pi$ (Figure 2) for an intensity modulator is often higher than the peak-to-peak voltage delivered by RF generators, so in this case it is necessary to amplify the electrical signals to obtain modulation signals compatible with the modulators specifications ($V\pi$). This is achieved by amplifier modules, often called modulator drive.

An acquisition of the data with a PC can be launched during operation to monitor the output optical power as well as the bias voltage. In operating conditions, the EO modulator has to be tested with respect to temperature (following the specifications of the manufacturer).

The optical transmission response of a MZ modulator in general is a function of the applied DC Bias Voltage, as sketched in Figure 2, and the key features to be characterized are four parameters related to the transfer curve of the MZ modulator [2]: The Insertion Loss, the Switching Voltage, the Extinction Ratio (ER) and the Nominal Operating Point. The Insertion Loss represent the optical loss at the maximum transmission point of the curve. The Switching Voltage $V_\pi$ is the difference in Bias Voltages at the Maximum and minimum transmission points. The ER is the ratio between the maximum and the minimum optical transmission levels [3-5], and the BIAS Operating Point is the voltage that results in optical transmission halfway between the minimum and maximum transmission levels. The MZ modulator response has to be linear for small deviations from the nominal oprating bias point.

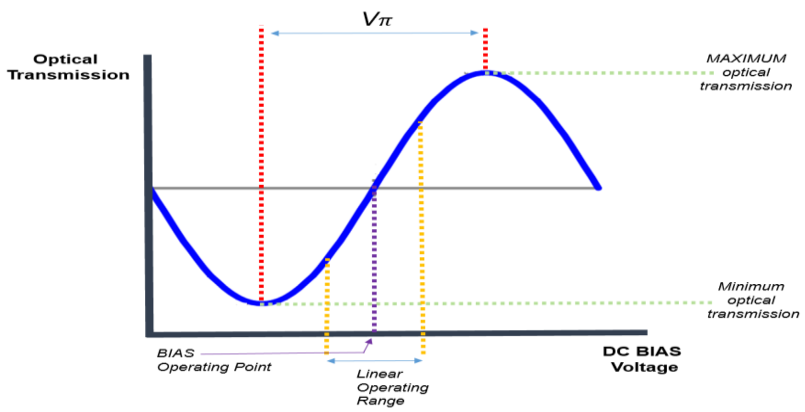


*Figure 2: MZ interferometer transmission transfer curve with respect to applied DC BIAS Voltage.*

The transfer function of an intensity modulator driven by a sinusoidal voltage, or in general variable in time (*V(t)*), and with a frequency $\omega$, can be written as:

$$I(t) = \tau_m \frac{I_{in}}{2}\left[1 + \cos\left(\pi \frac{V_{BIAS} + V_{pp}\, A(\omega)\cos(\,\omega t + \theta(\omega)\,)}{V_\pi}\right)\right] = \tau_m \frac{I_{in}}{2}\left[1 + \cos\left(\frac{\pi}{V_\pi}\, V(t) - \varphi\right)\right] \quad (1)$$

where $I_{in}$ represents the maximum Intensity transmitted; $\tau_m$ is the transmittivity of the waveguide; $V_{BIAS}$ , $V_{PP}$ and $V\pi$ are respectively the Bias voltage, the peak voltage applied to the modulator and its switching voltage; $A(\omega)$ is the modulation amplitude and $\theta(\omega)$ the phase. By varying the $V_{BIAS}$ it is possible to optimise the operating point on the transfer curve of the modulator.
The intensity modulators are designed to have equal arms: these balanced optical paths returns a phase term $\varphi$ theoretically equal to zero. Nevertheless, in practical implementations a small difference between the two branches of the interferometer are always present, generating the general phase term $\varphi$ in the equation of modulator function transfer reported above.
Concerning with the optical modulation depth measurement [2], the ratio between the peak optical modulated signal power and the average optical power, an oscilloscope platform can be used.
In figure 3 are reported examples of different configurations of the set-up described in Figure 1 to perform Extinction Ratio characterization and insertion loss measurement. In Figure 4 examples of typical signal at the output of the RF amplifier module (A) and at the output of the MZ intensity modulator (B) are reported.

Finally, it is worth to notice that during characterizatoin measurements a particular attention has to be paid to temperature isolation and control of the modulator, as well as to the deployment of the optical fibers, due to their sensitivity to mechanical stress, temperature variations and air flows.

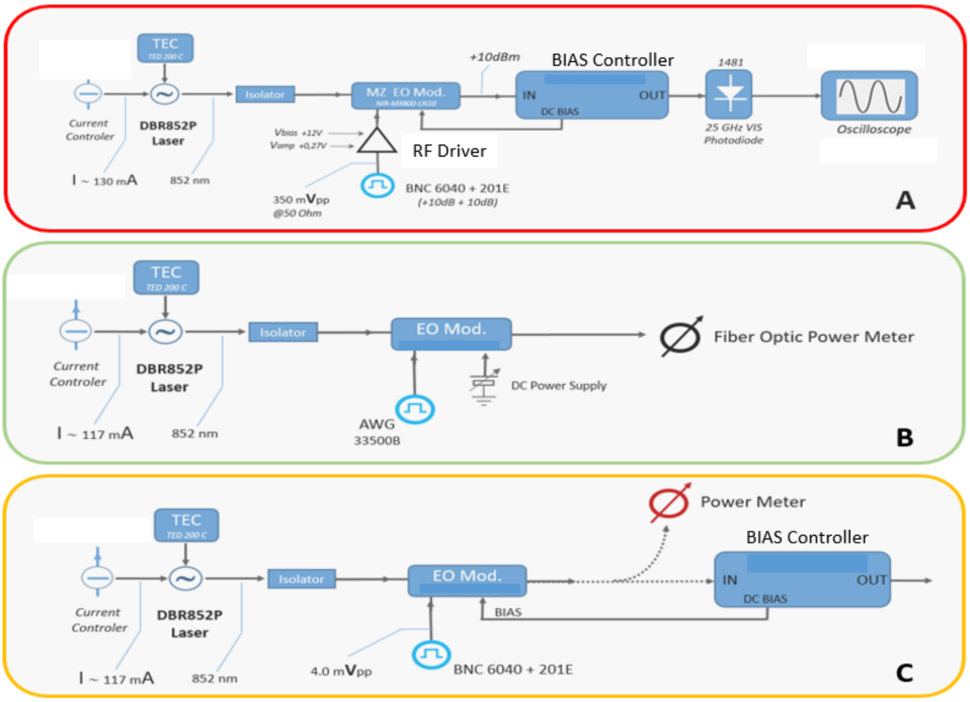


*Figure 3: Set-up implemented for characterization measurements of key parameters of intensity modulators (A-B: Extinction Ratio characterization set-up, respectively with and without Modulator Bias Controller; C: insertion losses measurement).*

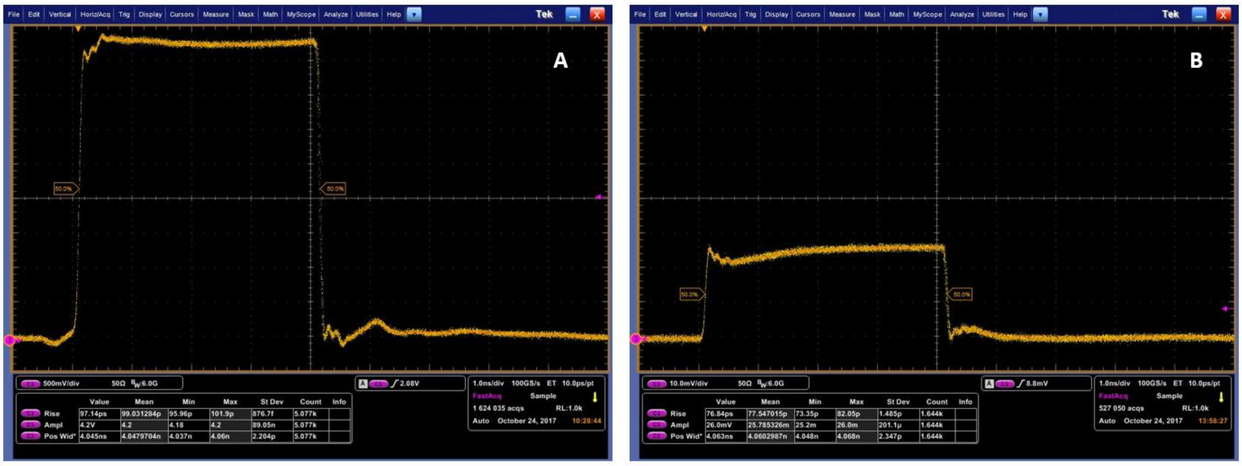


*Figure 4: A) Screen shot of a typical signal at the output of the RF amplifier module; B) Screen shot of a typical signal output from the MZ intensity modulator.*

## ***Reference***

[1] H.-K. Lo, M. Curty and K. Tamaki, Secure quantum key distribution, Nature Photonics, 8, 595 (2014).

[2] D. Derickson, Fiber Optic – Test and Measurement (1998, Prentice Hall PTR, USA).

[3] R. L. Jungerman, et al., High-Speed optical modulator for application in instrumentation, J. Lightwave Tech. 8, 1363 (1990).

[4] P. O. Anderson, et al., Accurate Optical Extinction Ratio Measurements, IEEE Photonics Technology Letters 6 (11), 1356 (1994).

[5] Optical interfaces for equipments and systems relating to the synchronous digital hierarchy." ITU-T Recommendation G. 957, International Telecommunication Union, Geneva, 1990.

## *How to characterize an attenuator used in free-space QKD systems with respect to transmission?*

### ***Introduction***

The best practice in characterisation of optical attenuators, typically used in some practical implementations of free-space QKD systems [1] to reduce the intensity of the coherent laser signal at the photon-counting regime, is reported in the following. For this purpose, some guidelines are prescribed for testing fibre optic digital attenuators. Typically, these kinds of devices present high resolution, high attenuation range and high-power handling, together with low insertion loss, low back-reflection, low polarization-dependent loss (PDL) and flat wavelength response. They operate by using interpolation between the calibration wavelengths, showing the capability of providing accurate attenuation levels over a continuous, broad range of wavelengths. Normally, the calibration can be operated at different wavelengths. In the spectral region of interest for free space QKD (namely the VIS-NIR region), manufactures use single wavelength sources at 830 nm, and the calibration is performed with a 0.01 dB resolution. This interpolation technique returns an attenuation precision of about 0.03 dB over the entire wavelength range of the device for up to 30 dB attenuation. Digital attenuators can be built using either single-mode, multimode or Polarization Maintaining (PM) fibre.

### ***Experimental implementation***

In stable environmental conditions, to perform the calibration, as illustrated in figure 1, a high-stable single-frequency cw-laser should be used. As a first step, the reference power is directly measured connecting the laser output with the calibrated power meter (direct connection between points A and B in figure 1). After that, the light from the transmission module is sent through the attenuator before entering the transmission line, optically guided in this case to the power measurement station. Once the attenuator under test is inserted, the power is measured setting 0 dB of attenuation on DUT, and the ratio between the two values, expressed in dB, is reported. Then the fibre optic attenuator under test is gradually stepped through a series of attenuation values. For any value of attenuation, the respective measured power is registered. In order to perform a reliable calibration, the power meter device has to be a standard meter presenting excellent linearity over the range of six or more decades, together with wavelength and polarization independence within the range of spectral responsivity.

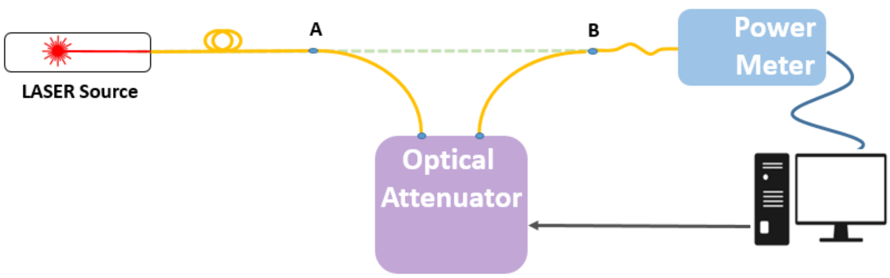


*Figure 1: Experimental implementation scheme of the facility for the characterization of a variable attenuator with respect to transmission (the measurement of the reference power is operated by direct connection of fibres ends in points A and B).*

The calibration must be performed aiming to reach the lowest uncertainty. Among the possible sources of uncertainty we list the following: nonlinearities of the calibration set-up; low stability of the laser source; optical interferences resulting in power fluctuations and due to back reflections within the optical guide path in concurrence with a source coherent length of the same order of magnitude as the distance between the reflection points; random fluctuations due to polarization dependence, thermal variations, air flow or mechanical stress over the fibres. It is highly recommended to fix all the fibres by taping them to the optical bench, and at the same time to thermally isolate them.

Due to the fact that the optical components used to implement this test procedure feature fibre pigtails with connectors on end and connectorized components, a particular attention must be paid to return loss and insertion loss measurement (for a detailed description, see ref [2]). It is highly recommended to design the calibration facility using the same type of optical fibres. Figure 2 shows an example of an attenuation curve with experimental data showing an excellent linear behaviour.

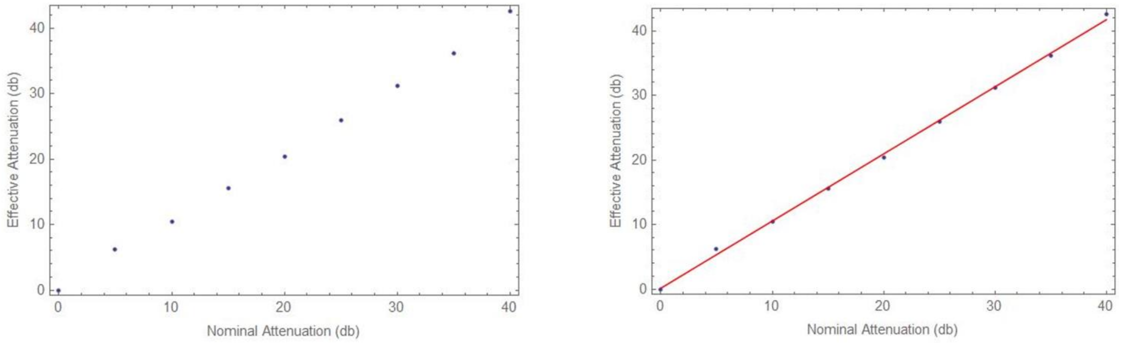


*Figure 2: Example of experimental data, with linear behaviour, obtained in the characterization of optical attenuators in fibre (diagram on the left) and the corresponding linear fit (on the right).*

## ***Reference***

[1] H.-K. Lo, M. Curty and K. Tamaki, Secure quantum key distribution, Nature Photonics, 8, 595 (2014).
[2] D. Derickson, Fiber Optic – Test and Measurement (1998, Prentice Hall PTR, USA).
[3] A. Ghatak, K. Thyagarajan, Introduction to Fiber Optics (1998, Cambridge University Press, UK).

## *Investigate the properties of the single-photon detectors (dark counts, deficiency, after-pulsing, dead-time etc.) used in quantum random number generators.*

An outstanding issue for QRNGs is authoritative accreditation of the output. Current tests are based on numerical analysis of the output sequence, which cannot provide a confident bound on the degree of randomness. Stronger certification is possible for physical QRNGs (PQRNGs), since the physical process used to create the output sequence can be theoretically analysed and physically tested.

The model developed in MIQC enabled entropy rates for a QRNG, based on a beam-splitter and two single-photon detectors, to be calculated as a function of detectors efficiency, dark count probability, and after-pulse probability. Work in this project focussed on developing robust methods to measure these properties of single-photon detectors. NPL and INRIM refined four methods for testing gated single-photon avalanche photodiodes. These methods have been documented in clause 15 of the ETSI Group Report “ETSI GS QKD 011 V1.1.1 (2016-05), Quantum Key Distribution (QKD); Component characterization: characterizing optical components for QKD systems” which was published by the Quantum Key Distribution (QKD) ETSI Industry Specification Group (ISG) [1]. The document is available to be freely downloaded from the ‘standards’ tab at https://www.etsi.org/technologies-clusters/technologies/quantum-key-distribution .

Additionally, NPL adapted method 4, where a pulsed laser is used to illuminate every nth detector gate and time-tagging of detector output pulses is employed, to the case of a free-running detector.

The free-running detector was an IdQuantique ID230, which is a cooled, free running, fibre-coupled detector system for use at telecom wavelengths with user-selectable set-points for temperature, efficiency, and detector dead time. The detector can be biased at different levels corresponding to factory-calibrated detection efficiency of 25%, 20%, 15%, or 10% at 1550 nm.

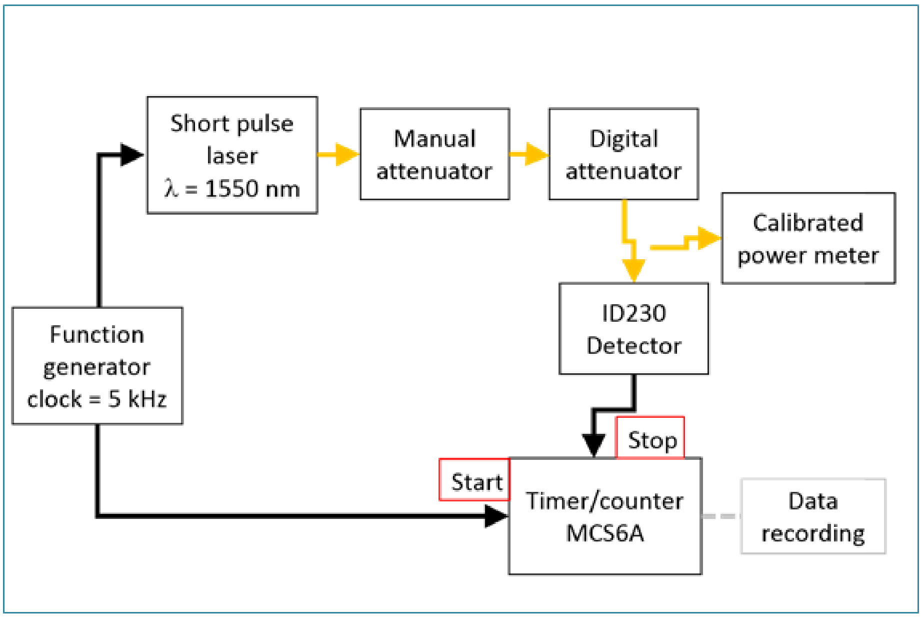


*Figure 1. Set-up to characterise the ID230*

Mean photon numbers between 0.02 and 4.0 were employed, and the detection efficiency was found to vary between (22.7 ± 2.1)% and (24.4 ± 0.8)%, the dominant source of uncertainty being due to setting the mean photon number.

| $\mu$ | $\eta$ (%) |
|---|---|
| 3.941 | $24.4 \pm 0.8$ |
| 1.246 | $24.0 \pm 0.9$ |
| 0.394 | $24.8 \pm 1.7$ |
| 0.125 | $23.9 \pm 1.7$ |
| 0.039 | $24.9 \pm 1.4$ |
| 0.017 | $22.7 \pm 2.1$ |

*Table 1. Measurement results. The uncertainty is dominated by the uncertainty (1%) in setting the incident mean photon number.*

*Additional details will be included in a future update after the technique has been published in the open literature.*

## ***Reference***

[1] ETSI Group Report "ETSI GS QKD 011 V1.1.1 (2016-05), Quantum Key Distribution (QKD); Component characterization: characterizing optical components for QKD systems": https://www.etsi.org/technologies-clusters/technologies/quantum-key-distribution.

# New components for free-space QKD systems and their characterisation

## *How to measure the linearity and the detection efficiency of few-photon detectors using synchrotron radiation?*

### *Introduction: Traceability for single photon radiometry by means of synchrotron radiation*

At the Metrology Light Source (MLS), the dedicated electron storage ring of the Physikalisch-Technische Bundesanstalt (PTB), the necessary equipment is installed to vary the electron beam current from 1 pA (one stored electron) to 200 mA [1]. The spectral radiant power of synchrotron radiation is directly proportional to the stored electron beam current, i.e. the number of stored electrons, and can be calculated from basic electrodynamic relations. Thus, the emitted spectral radiant power can be varied from a few attowatts, i.e. a few photons per second, to milliwatts of radiant power depending on the actual experimental conditions. The MLS has been used recently to calibrate free-space and fibre-coupled single photon detectors traceable to the cryogenic radiometers of PTB [2,3].

### *The calibration method*

Schematics of the setups used to calibrate a fibre-coupled superconducting nano-wire single photon detector (SNSPD) and Silicon single photon counting (Si-SPCM) modules are shown in Fig. 1. The photon rate ($PRI_{\mathrm{high}}$) in the high ring current range is measured, depending on the wavelength of the radiation, by a calibrated InGaAs reference detector or a calibrated trap detector using their known spectral responsivity. In a second step the count rate of the SNSPD $CR_{\mathrm{SNSPD}}$ or Si-SPCM $CR_{\mathrm{SPCM}}$ is measured in the low ring current range. The uncorrected detection efficiency of the SNSPD or SPCM $DE*$ can then be calculated. With this calibration method combined relative standard uncertainties as low as 0.16 % for free-space detectors (see Table 1) and 2 % for fibre-coupled detectors have been achieved.

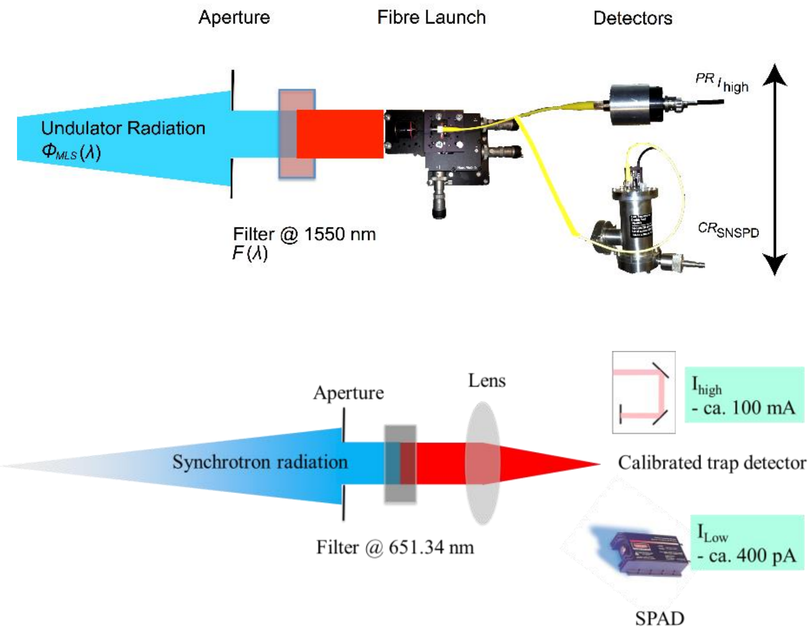


*Figure 1a,b: Calibration schemes for fibre-coupled and free-space single photon detectors.*

*Table 1: Uncertainty budgets for the calibration of two free-space Silicon single photon counting modules by means of synchrotron radiation traceable to the cryogenic radiometer.*

| Source of uncertainty | Correction factor | SPAD1 | SPAD2 |
|---|---|---|---|
| Count rate Si-SPCM normalized to ring current | | 0.049 % | 0.047 % |
| Ratio photocurrent trap detector to ring current, Type A | | 0.051 % | 0.051 % |
| Ring current measurement | | 0.048 % | 0.048 % |
| Spectral responsivity | | 0.045 % | 0.045 % |
| Detector positioning | | 0.020 % | 0.020 % |
| Bandwidth | 1.0004 | 0.019 % | 0.019 % |
| Detector sizes | 1.035 | 0.09 % | 0.09 % |
| Statistic | 1.00018 | 0.018 % | |
| | 1.00018 | | 0.018 % |
| Afterpulsing | 0.998571 | 0.098 % | |
| | 0.999333 | | 0.071 % |
| **Combined uncertainty** | | **0.17 %** | **0.16 %** |

## ***A few-photon detector based on the Predictable Quantum Efficient Detector***

The few-photon detector is based on the principle of the Predictable Quantum Efficient Detector (PQED) [4,5] and, hence, the detector can be used with radiant power levels from approximately 300 µW down to the detection limit. However, the PQED has been shown to be linear down to photocurrents below 1 nA limited by the detectivity of the linearity measurement facility used in [5] only. The spectral responsivity of the PQED is given by $R(\lambda) = \frac{e\,\lambda}{h\,c}(1-\rho(\lambda))(1-\delta(\lambda))$. The factor $\frac{e\,\lambda}{h\,c}$ is the responsivity of an ideal quantum detector expressed by fundamental constants and the vacuum wavelength $\lambda$ of the applied radiation. The parameters $\rho(\lambda)$ and $\delta(\lambda)$ describe the spectrally dependent reflectance and internal quantum deficiency (IQD) respectively. If these parameters are known, the spectral responsivity of the few-photon PQED can be predicted. The few–photon PQED is made from a single custom-made induced junction photodiode produced within the EMRP-JRP "NEWSTAR - New Primary Standards and Traceability for Radiometry". The internal quantum deficiency of the few-photon PQED has been determined according to the prediction presented in [6]. The reflectance of the single diode at a wavelength of 850 nm has been calculated and measured by means of a collimated laser beam.

The few-photon Predictable Quantum Efficient Detector (PQED) is based on a single induced-junction photodiode. The general design of the detector is shown in Fig. 2. The photodiode has been produced within the project EMRP SIB57 "NEWSTAR". The photodiode is mounted under an angle of 45°, close to Brewster's angle to minimize the reflection losses for p-polarized radiation. The photodiode and the amplifier stage are attached to the cooled and temperature stabilized base-plate of the detector assembly. The aperture of the detector is exchangeable to match with the active diameter of the devices under test, typically single photon counting modules have active diameters between 0.15 mm and 0.5 mm. Here, a 210 µm pinhole was used to match the active area of two Perkin & Elmer SPCM used at PTB. The few-photon PQED can be used as a detector standard when its losses, i.e. its external quantum deficiency, are known.

### **Design of the few-photon PQED**

The detector can be used with radiant power levels from approximately 300 µW down to the detection limit. To minimize the lower detection limit, the detector is actively cooled and a low-noise switched integrator current amplifier (SIA) is installed next to the photodiode and on the same temperature controlled base plate. In addition to the SIA a low noise current amplifier was developed at PTB providing gains from $10^{10}$ to $10^{12}$. This amplifier can supply a small bias voltage with µV resolution to minimize the dark current. The housing can be purged with dry nitrogen in order to prevent condensation on top of the photodiode. The photodiode is mounted under an angle of 45° relative to the incoming beam. This configuration, that is close to Brewster's angle, reduces the reflection losses to approximately 10 % for p-polarized radiation at 850 nm. The inside of the detector is all black, which reduces the relative false light level below 1 %. However, while the internal quantum efficiency can be calculated using sophisticated software models and is higher than 0.9999 in the range from 400 nm to 800 nm [3], the calculation of the reflectance is more difficult because the actual thicknesses of the $SiO_2$-layers have to be known precisely. The calculated reflectance for the given configuration changes from 10% for a $SiO_2$ thickness of 190 µm to 15% for a $SiO_2$ thickness of 250 µm.

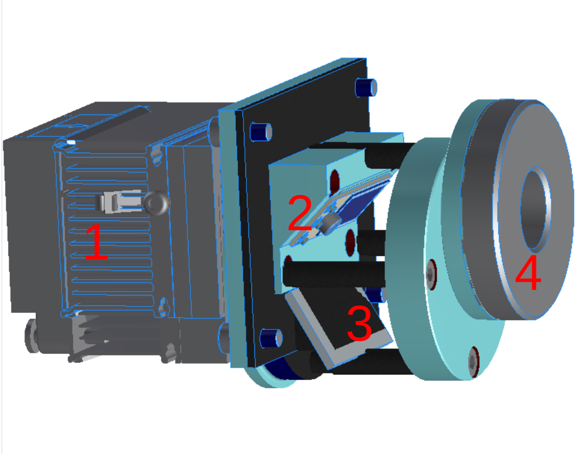


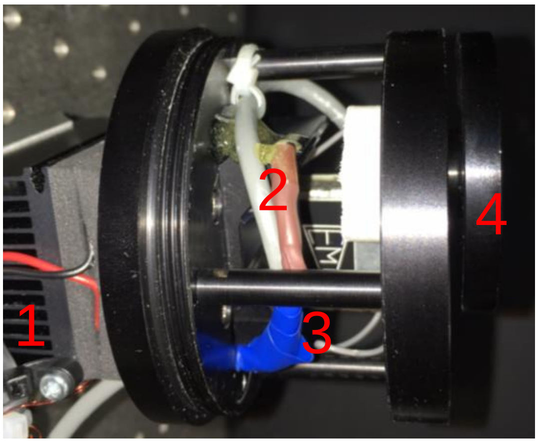


*Figure 2: CAD-drawing (left side) and photograph (right side) of the few-photon PQED. The radiation enters the detector through an exchangeable pinhole that can be used to match the active areas of the few-photon PQED and the device under test.*
*1 TE-cooler, 2 PQED-photodiode, 3 „mirror", 4 210 µm pinhole*

**Linearity measurements**

Figure 3 shows the results of the linearity measurements, was performed by means of synchrotron radiation.

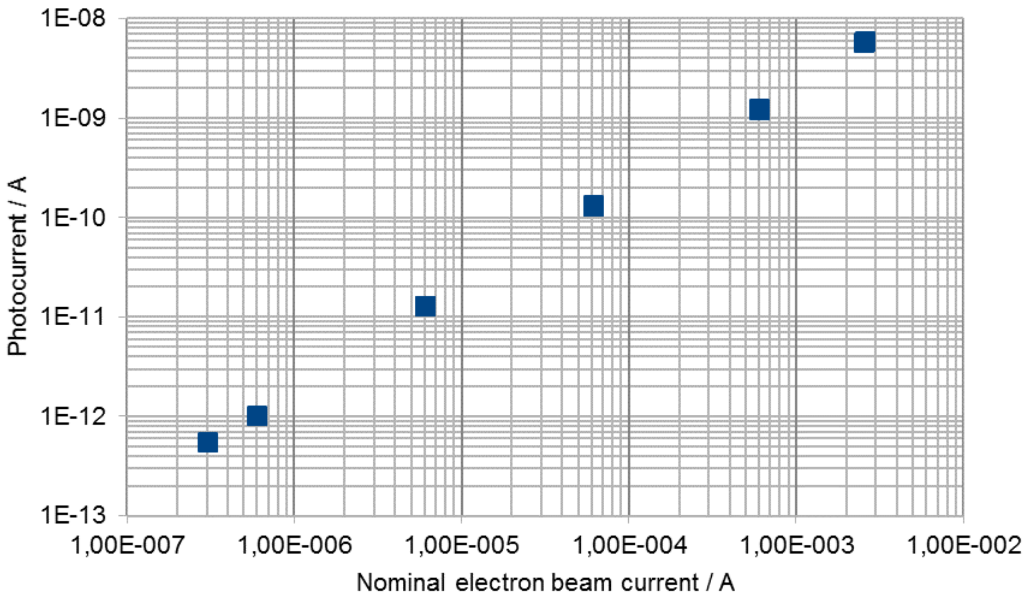


*Figure 3. Measured linearity of the few-photon PQED equipped with a switched integrator amplifier. This test was performed by means of synchrotron radiation.*

**Detection efficiency measurements**

The results of the measurements and the different detection efficiencies obtained with a calibrated trap detector and the few-photon PQED at the nominal wavelength of 850 nm are shown in Table 2. The detection efficiencies measured against the trap and the few-photon PQED differ by 0.002. The relative standard uncertainty of the detection efficiency of the SPCM measured with the few-photon PQED is 1.9 % with the uncertainty associated with the linearity of the spectral responsivity being the dominant source of uncertainty. For typical calibration conditions, a relative standard uncertainty of 2 % to 3 % could probably be achieved.

*Table 2: Comparison of detection efficiencies of a SPCM at 850 nm measured by means of a calibrated trap detector and the few-photon detector.*

| | **Trap** | **Few-photon PQED** | **SPCM** | $DE_{\mathrm{Trap}}$ **-** $DE_{\mathrm{SPCM}}$ |
|---|---|---|---|---|
| $\boldsymbol{\Phi_{e^-}}$ | 13.949 ± 0.005 | 13.90 ± 0.16 | | |
| $C_{\mathrm{SPCM}}$ **per** $e^-$ | | | 7.783 ± 0.005 | |
| **Detection efficiency SPCM** | 0.5580 ± 0.0023 | 0.556 ± 0.010 | | 0.002 |

## ***References***


[1] R. Klein, R. Thornagel, G. Ulm, From single photons to milliwatt radiant power—electron storage rings as radiation sources with a high dynamic rang,e Metrologia 47, R33-R40 (2010).

[2] Müller, I., Klein, R., Hollandt, J., Ulm, G. and L. Werner (2012). Traceable calibration of Si avalanche photodiodes using synchrotron radiation. Metrologia, 49, 152–155.

[3] Müller, I., Klein, R., and Werner, L. (2014). Traceable calibration of a fiber-coupled superconducting nano-wire single photon detector using characterized synchrotron radiation. Metrologia 51 S329 (2014)

[4] Sildoja et al., Metrologia 50 (2013) 385

[5] Müller et al., Metrologia 50 (2013) 395

[6] Gran et al., Metrologia 49 (2012) S130